University of Miami
Scholarly Repository

Open Access Theses | Electronic Theses and Dissertations

2016-07-30

# Integrated Biocompatible Piezoelectric Micropump System with Nanoliter Volume Precision

Yagmur Akin
*University of Miami*, yagmurakin89@gmail.com

Follow this and additional works at: https://scholarlyrepository.miami.edu/oa_theses

Recommended Citation
Akin, Yagmur, "Integrated Biocompatible Piezoelectric Micropump System with Nanoliter Volume Precision" (2016). *Open Access Theses*. 617.
https://scholarlyrepository.miami.edu/oa_theses/617

This Open access is brought to you for free and open access by the Electronic Theses and Dissertations at Scholarly Repository. It has been accepted for inclusion in Open Access Theses by an authorized administrator of Scholarly Repository. For more information, please contact repository.library@miami.edu.

UNIVERSITY OF MIAMI

# INTEGRATED BIOCOMPATIBLE PIEZOELECTRIC MICROPUMP SYSTEM WITH NANOLITER VOLUME PRECISION

By

Yagmur Akin

A THESIS

Submitted to the Faculty
of the University of Miami
in partial fulfillment of the requirements for
the degree of Master of Science

Coral Gables, Florida

August 2016

©2016
Yagmur Akin
All Rights Reserved

UNIVERSITY OF MIAMI

A thesis submitted in partial fulfillment of
the requirements for the degree of
Master of Science

# INTEGRATED BIOCOMPATIBLE PIEZOELECTRIC MICROPUMP SYSTEM WITH NANOLITER VOLUME PRECISION

Yagmur Akin

Approved:

| | |
|---|---|
| _____ | _____ |
| Onur Tigli, D.Sc.<br>Associate Professor of<br>Electrical and Computer Engineering | Mei-Ling Shyu, Ph.D.<br>Professor of<br>Electrical and Computer Engineering |
| _____ | _____ |
| Ali Ghahremaninezhad, Ph.D.<br>Assistant Professor of<br>Civil, Architectural & Environmental Engineering | Guillermo Prado, Ph.D.<br>Dean of the Graduate School |

AKIN, YAGMUR (M.S., Electrical and Computer Engineering)

(August 2016)

Integrated Biocompatible Piezoelectric Micropump System with Nanoliter Volume Precision

Abstract of a thesis at the University of Miami.

Thesis supervised by Dr. Onur Tigli.
No. of pages in text. (71)

Developments in microfluidics have led a wide variety of research on MEMS-scaled biomedical applications. Many biomedical sensors, drug delivery systems, cell and protein syntheses devices, microfluidic switches have been successfully miniaturized. However, there is a need for controlled fluid transport for most of these biomedical devices. To address this need, micropump design has been a highly attractive research area for decades and various micropump design templates have been used for controlled fluid transfer. However, most of these developed micropumps are either: not small enough to combine with other microfluidic systems or require a large activation energy which does not make them suitable for biomedical applications.

This thesis presents a fully biocompatible micropump system consisting of a new actuator membrane structure fabricated from a piezoelectric polymer: polyvinylidene fluoride-trifluoroethylene (PVDF-TrFE). Its actuating performance was evaluated and compared with other common piezoelectric materials using finite element method (FEM) simulations.

Full operation of actuator-membrane structures and diffuser elements which are the two components of the designed micropump were successfully proven separately and integration of these components was demonstrated.

**Acknowledgements**

First off all, I would like to thank my advisor Dr. Onur Tigli. I have gained valuable experience under his supervision. His professional approach to his students and highly motivated team were my guiding spirit during graduate school. I feel privileged to be a member of his research group.

Special thanks to the Turkish Ministry of Education for funding my graduate education at University of Miami.

I would like to thank to the committee members Prof. Mei Ling Shyu and Prof. Ali Ghahremaninezhad, and extend my thanks to all my lab-mates. It was a great opportunity to have an extremely talented colleague like Dr. Sukru Ufuk Senveli who never stops having new ideas and sharing them with us. I could not have done this work if Alperen Toprak was not supporting me with his enormous knowledge in the field. I received great help with microfluidic experiments from Randil Gajasinghe who is the kindest colleague I have ever met. I would also like to acknowledge Jorge Gomez for his support and experience. I would like to give a special thanks to the last member of our group, my husband who was always next to me with his calming smile, interminable support, and patience. Additional thanks to our supervisor Dr. Tigli for giving us the opportunity of working together, I could not imagine our marriage otherwise.

I am indebted to my friends Gokce Toprak and Duygu Yasar for embellishing my life outside of the research.

My parents Sultan, Baki, and my siblings Meliha, Umay, and Afsin Akin deserve the greatest thanks and acknowledgement for their moral and financial support, and above all, trust and encouraging attitude.

Finally, as a member of the Tigli BioCMOS/MEMS/NANO lab at University of Miami, I would like to gratefully acknowledge the support from the National Science Foundation (NSF) under grant No. ECCS-1349245.

**TABLE OF CONTENTS**

## LIST OF TABLES

**LIST OF FIGURES**

# CHAPTER 1. INTRODUCTION

## 1.1. Motivation

Developments in microfluidics have led a wide variety of research on MEMS-scaled biomedical applications. Many biomedical sensors, drug delivery systems, cell and protein syntheses devices, microfluidic switches have been successfully miniaturized. However, there is a need for controlled fluid transport for most of these biomedical devices. To address this need, micropump design has been a highly attractive research area for decades and various micropump design templates have been used for controlled fluid transfer. However, most of these developed micropumps are either: not small enough to combine with other microfluidic systems or require a large activation energy which does not make them suitable for biomedical applications.

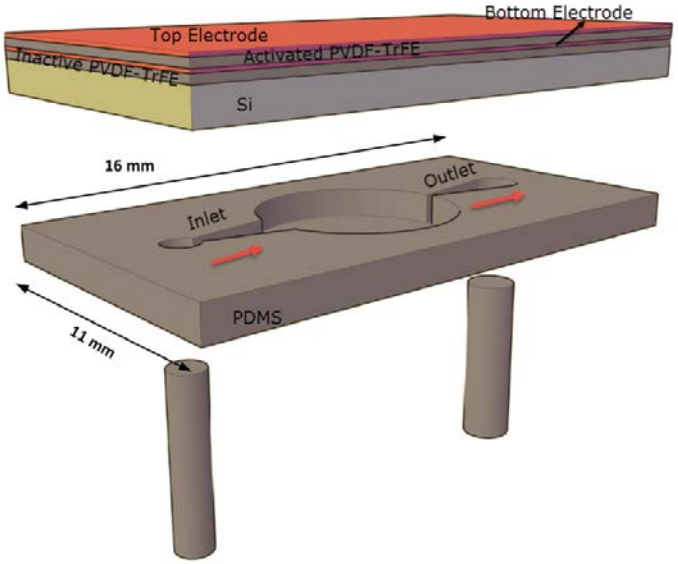


**Figure 1.1: 3D schematic of the proposed micropump. Actuator and membrane structures were fabricated on a silicon substrate and suspended by silicon etching. The diffuser valves and the chamber were built in the sealing PDMS.**

Most of the micropump systems consist of a microfluidic channel, fluid actuator and fluid directing elements. Micropumps that provide fluid actuation are the most challenging components for biomedical microfluidic devices due to their low efficiencies, high voltage requirement, and non-precise output. The object of this research was to build a miniaturized fully biocompatible micropump system consisting of fluidic channels and fluid directing elements that can precisely deliver a nanoliter volume of fluidic sample to implantable high precision therapeutic drug transfer devices. The schematic of the designed micropump is shown in Figure 1.1.

**1.2. What are the challenges of the presented study?**

Microfluidic devices are a great development for biomedicine. They bring time, cost, and sample efficient perspective into the biomedical research. However, fluidic behavior is very complicated at micro scale. Gas trapping in microchannels is one of the major problems that all researchers in this field deal with. While strong bonding between the actuation and fluidic sections helps to reduce trapped gas, surface treatment is sometimes needed to reduce surface tension.

Operating voltage is another challenge. Low voltage (2-20V) is required since these micropumps are designed to be used mostly for medical applications. While this is not a problem for macro-scaled devices, it is quite challenging to achieve the desired flow outputs at low voltages for micro-scaled devices. Additionally, it is very difficult to precisely control the nanoliter volume mechanically.

### 1.3. What was accomplished in this work?

- Finite element analyses of actuator-membrane systems were studied using common materials in literature. Polydimethylsiloxane (PDMS), poly-methyl-methacrylate (PMMA), silicon dioxide ($SiO_2$) were used for the membrane structure, and lead zirconium titanate (PZT), zinc oxide (ZnO) and polyvinylidene fluoride-trifluoroethylene (PVDF-TrFE) were used for the actuator structure. The results were compared in order to find optimal materials. Both the effects of diameter and thickness changes of the actuator were studied. Additionally, the residual stress, which can be caused by lattice mismatch and temperature coefficient of expansion (TCE), was taken into account.
- A novel actuator-membrane structure from PVDF-TrFE thin film was successfully fabricated and the fabrication processes were reported.
- Full operation of each section of the micropump system, which includes the actuator-membrane structure as the fluidic actuator and diffuser / nozzle elements as the fluid directing element, was successfully demonstrated separately. Integration of these two sections and testing of the integrated devices were presented. However, the integrated system could not be successfully tested due to some practical challenges which can be eliminated by further research.

### 1.4. Microfluidics

Microelectromechanical systems (MEMS) provide a prospect of producing small devices using microfabrication techniques. This has resulted in extended research into wide variety of fields – such as smart devices, automotive industry, textile, and medicine. Biomedical industry has become one of the most popular sectors that use MEMS

technologies through the use of microfluidics. Microfluidics deal with design and development of small scale devices [2]. This can aid in diagnostic procedures, drug delivery, and related research such as cell manipulation and culture, analysis of viruses, and other malicious entities. Many laboratory analysis procedures require time consuming repetition of numerous tests. Microfluidic technology not only reduces the size of the equipment, but also produces solutions to this issue. With the development of microfluidic systems, analysis time and required sample volume can be reduced dramatically [3]. Many microfluidic studies have been accomplished, and various devices have been reported since MEMS became popular. Some of these include: implantable drug delivery, sequencing or synthesis of nucleic acids, cell immobilizing and separation, coolants and moreover. While each application requires different elements, all have a common need: mechanism of fluid transportation. This thesis presents a novel micropump designed for fluid transportation in biomedical applications.

### 1.5. Micropumps

Micropumps and microvalves are the most crucial components in microfluidic systems and found in chemical analysis, biological or chemical sensing, drug delivery, protein synthesis, and genetic engineering. Polla et al. reported that micropumps can pump metered amounts of drugs into a microneedle system, which is suitable for delivering modern biological drugs that cannot be delivered by traditional delivery methods [4]. After the first MEMS-based micropump was developed for insulin delivery systems in order to maintain blood sugar level of diabetic patients by Smits in 1984 [5], thousands of studies have been reported and many types of micropumps have been fabricated. These MEMS-based micropumps were usually classified as mechanical and

non-mechanical micropumps [2, 6-8] or displacement/dynamic [9]. Mechanical micropumps need a physical actuator or mechanism to perform pumping action while the non-mechanical types transform certain available non-mechanical energy into kinetic momentum [8]. In this thesis, mechanical micropumps are also categorized according to their actuation and displacement method for better understanding in the following subsections.

In general, a micropump must be designed to optimize some performance parameters including maximum flow rate $Q_{max}$ (obtained when the pump is working at zero back pressure), maximum back pressure $p_{max}$ (measured when the flow rate of the pump is at zero), pump power $P_{pump}$, and pump efficiency $\eta_{pump}$. The pump efficiency can be calculated using Eq.1.

$$\eta_{pump} = \frac{P_{pump}}{P_{actuator}} \quad \text{(Eq.1)}$$

The power transferred to the fluid by the pump, $P_{pump}$, is the product of specific weight, discharge, and net head change. It can be expressed as;

$$P_{pump} = p_{max} Q_{max} = \rho g Q_{max} h_{max} \quad \text{(Eq.2)}$$

The pump head ($h$) can be calculated from the steady flow energy equation by neglecting viscous work and heat transfer, and assuming incompressible fluid flow.

$$h = \left(\frac{p}{\gamma} + \frac{u^2}{2g} + z\right)_{out} - \left(\frac{p}{\gamma} + \frac{u^2}{2g} + z\right)_{in} \quad \text{(Eq.3)}$$

where $\gamma = \rho g$ is specific weight of fluid, $g$ is acceleration of gravity, ρ is the fluid density, $u$ is velocity, and $z$ is elevation.

The maximum pump head can be rewritten as Eq.4 by assuming the inlet and outlet velocities and elevations are same [10].

$$h_{max} \approx \frac{p_{out} - p_{in}}{\gamma} = \frac{\Delta p}{\gamma} \quad \text{(Eq.4)}$$

### 1.5.1. Mechanical Micropumps

Mechanical micropumps require a physical actuator or a mechanism to carry out fluid transportation. Mechanical micropumps can be further classified into two groups according to their actuation or displacement methods.

**Classification by Actuation Methods**

All mechanical micropumps require an actuator regardless of type in order to generate mechanical energy to transfer the flow [3]. These actuators can be integrated or bonded as an external component according to the fabrication methods and application needs. Actuators of micropumps may utilize electrostatic, electromagnetic, thermo-pneumatic, shape memory, bimetallic, ionic conductive, and piezoelectric properties.

***Electrostatic***

Electrostatic actuation occurs when two parallel plates are charged oppositely. This is also known as Coulomb's law – force of attraction. The membrane is deflected by the electrostatic actuation force when a voltage is applied and returns its initial position once the applied voltage is cut off.

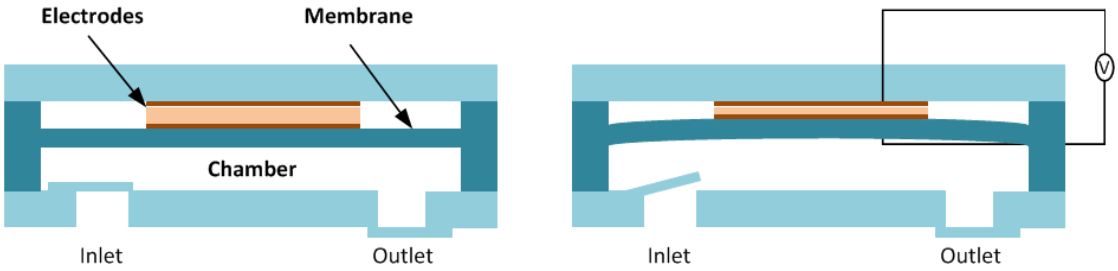


**Figure 1.2: Schematic of the initial position (left) and supply mode (right) of an electrostatic micropump. The figure adapted from [2].**

The generated electrostatic actuation force between two parallel plates can be expressed as;

$$F = \frac{dW}{dx} = \frac{\varepsilon A V^2}{2d^2} = \frac{\varepsilon_0 \varepsilon_r A V^2}{2d^2} \qquad \text{(Eq.5)}$$

where $F$ is the electrostatic actuation force, $W$ is the stored energy, $\varepsilon_0$ is the permittivity of free space , $\varepsilon_r$ is the relative permittivity of the material, $A$ is the overlapping area of the plates, $V$ is the applied voltage, and $d$ is the distance between two parallel plates. The advantages of electrostatic micropumps are low power consumption and easily controllable displacement whereas the major disadvantages are small membrane displacements and fabrication challenges.

***Electromagnetic***

An electromagnetic micropump usually consists of permanent magnets and micro coils as one of them attached to the membrane. A magnetic field is generated when current passes through the coils. The interaction between permanent magnets and the magnetic field generated by micro coils produces electromagnetic force. This force forms membrane deflection, resulting in pumping action.

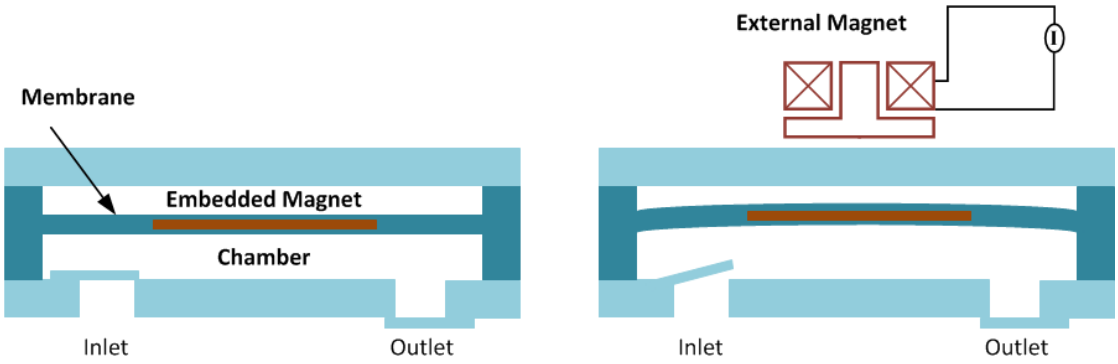


**Figure 1.3: Schematic of the initial position (left) and supply mode (right) of an electromagnetic micropump. The figure adapted from [2].**

The electromagnetic force $F$ can be expressed as;

$$F = (IxB)L \qquad \text{(Eq.6)}$$

where $I$ is the current passing through the coils, $B$ is the magnetic field, and $L$ is the length of the wire. This type of pumps can provide large actuation forces, hence large displacement with low operating voltages. However, the size cannot be reduced easily since an external magnet is required. Additionally, the current passing through the coils generates heat which is not suitable for the heat sensitive applications.

***Thermo-pneumatic***

A thermo-pneumatic actuator usually consists of a heater, a diaphragm and a sealed cavity. The actuation is based on thermally induced volume or phase change of sealed fluid in a chamber. When a voltage is applied to the heater, air volume inside the cavity increases, thus the pressure increases inside the channel. Similarly, with other membrane-type pumps, the periodical volume change in the chamber results in pressure change, herewith pumping action.

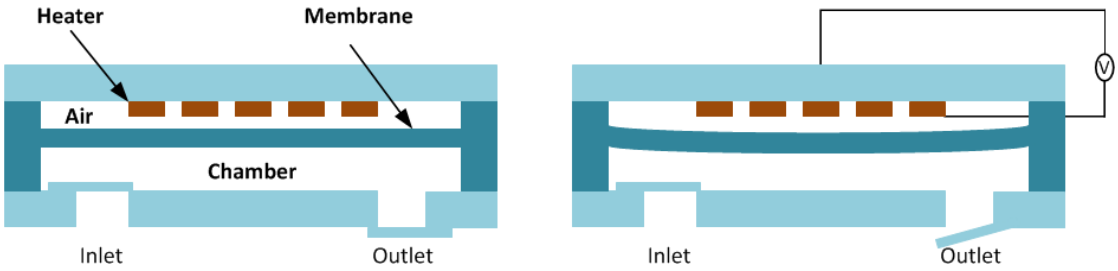


**Figure 1.4: Schematic of the initial position (left) and pump mode (right) of a thermo-pneumatic micropump. The figure adapted from [2].**

The pressure change ΔP can be expressed as;

$$\Delta P = E(\beta \Delta T - \Delta V/V) \quad \text{(Eq.7)}$$

where $E$ is the modulus of elasticity, $\beta$ is the thermal expansion coefficient, $\Delta T$ and $\Delta V$ are temperature and volume changes, respectively. These types of pumps require high power consumption and show slow response time. Additionally, actuation by heat is not suitable for applications where temperature change is critical.

***Shape memory alloy (SMA)***

Shape memory alloy (SMA) actuated micropumps use the shape memory effect in SMA materials such as titanium-nickel (Ti/Ni), gold-copper (Au/Cu), and titanium-indium (Ti/In) [7]. These alloys inherit a useful material property that is capable of restoring its initial shape after each heating/cooling cycle. SMAs change their phases from Martensite phase into Austensite phase after being heated. This phase transformation results in shape deformation on the membrane and pressure change inside the chamber. SMA-type micropumps require high power consumption and show slow response similar to thermo-pneumatic micropumps.

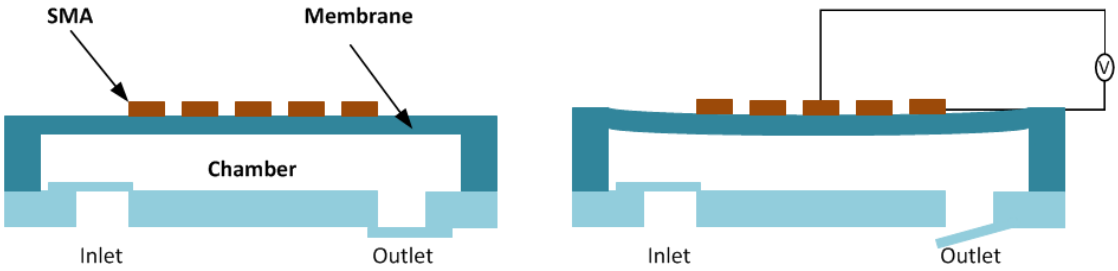


**Figure 1.5: Schematic of the initial position (left) and pump mode (right) of a shape memory alloy micropump. The figure adapted from [2].**

***Bimetallic***

Bimetallic actuators consist of two materials that have different thermal expansion coefficients. When these dissimilar materials are bonded together and heated, the deflection of the membrane is induced against thermal alternation [8]. This type of actuators can also be used as membranes shown in Figure 1.6 or can be bonded on top of a membrane. The displacement depends on directly the dissimilarity ratio of the actuator materials. These types of micropumps are also show slow response.

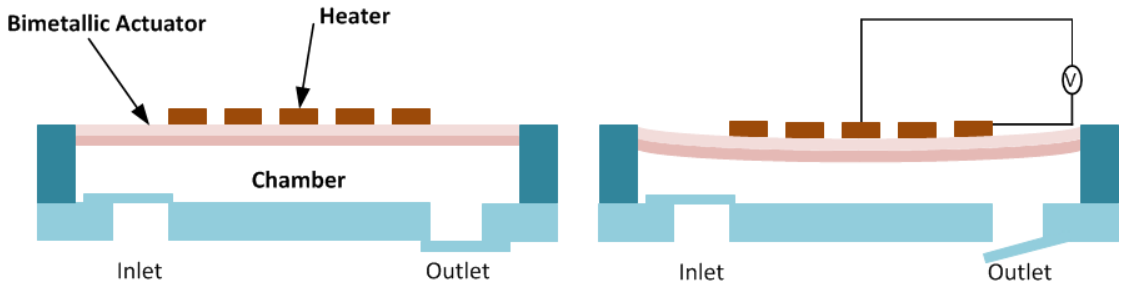


**Figure 1.6: Schematic of the initial position (left) and pump mode (right) of a bimetallic micropump. The figure adapted from [2].**

***Ionic conductive polymer film (ICPF)***

ICPF actuators consist of a polymer whose two sides are deposited with highly conductive thin films such as gold. Basically, these two thin films serve as the metal electrodes and pull ions along two sides of the polymer. When a voltage is applied, this

movement of the ions results in bending of the polymer membrane. Advantages of the ICPF actuators include: large displacement, low power consumption, and biocompatibility.

***Piezoelectric***

Piezoelectric micropumps are actuated by reverse piezoelectric effect which is a generated mechanical strain from an applied electrical field. This type of micropumps are the most widely used displacements micropumps because of their high displacement capacity and fast response [2]. A piezoelectric micropump usually consists of a membrane, piezoelectric disk attached on the membrane, and fluid chamber. However, studies in recent years show that thin film piezoelectric materials can be deposited on top of the membrane by using traditional microfabrication methods [11-13].

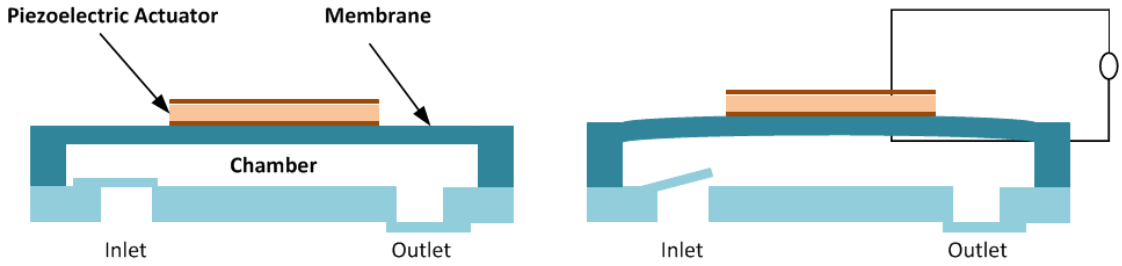


**Figure 1.7: Schematic of the initial position (left) and supply mode (right) of a piezoelectric micropump. The figure adapted from [2].**

Simple structure and fast response time are the advantages of using piezoelectric micropumps whereas the most common drawback is the high actuation voltage requirement for desired amount of displacement. However, the power consumption can be reduced by using thin film actuators. In this thesis, a membrane-type micropump with piezoelectric thin film actuator was fabricated using classic microfabrication processes. Information in detail about the piezoelectric micropumps is given in the next chapter.

## Classification by Displacement Methods

### *Diaphragm/Membrane*

The most popular micropumps are membrane-type micropumps. All the previously discussed actuator methods fall into this category. Membrane-type micropumps consist of a flexible membrane, pump chamber, actuator, and fluid directing elements such as check valves or diffuser / nozzle elements. A simple schematic of a membrane-type micropump is given in Figure 1.8.

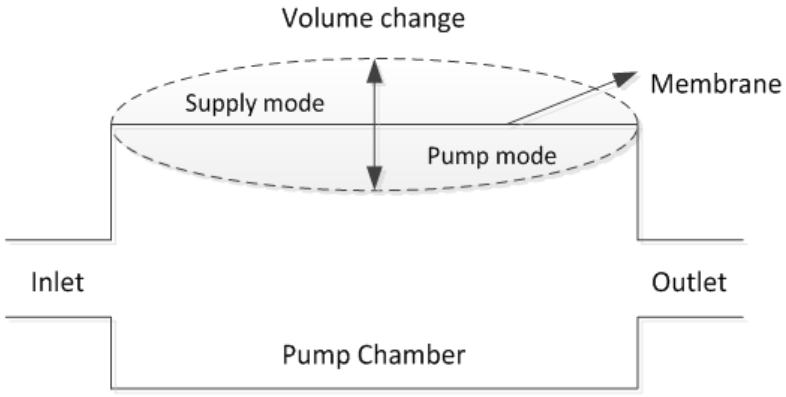


**Figure 1.8: Illustration of a membrane-type micropump. An actuator has to be attached to the membrane in this type of micropumps, and fluid directing elements are placed to inlet and outlet to prevent the reverse flow. Pump works at supply mode when displacement of the membrane is positive. During this mode, volume inside the chamber increases resulting in pressure decrease. Pump works at pump mode when displacement of the membrane is negative, and volume decreases resulting in pressure increase while this movement.**

There are many studies in literature about membrane-type micropumps. A silicon membrane micropump was used with a lead zirconium titanate (PZT) actuator and diffuser elements by Johari et al. in 2011, and a flow rate of 4.98 nL/min at 673 Hz was reported [14]. Zhou and Amirouche fabricated an all-PDMS membrane-type valveless micropump that is actuated by micromagnets, and 319.6 μm/min flow rate was

reported [15]. Another PDMS membrane valveless micropump activated by a PZT disk was developed in 2015, and 20 μm/min flow rate was reported at 200 Hz and 30 V by Singh et al. [16]. A rubber membrane micropump actuated by PZT sheets was studied by Wang et al. in 2014, and 118 ml/min flow rate at 361 Hz was reported [17]. A PET membrane was used in 2014 with polyvinylidene fluoride-trifluoroethylene (PVDF-TrFE) piezoelectric actuator and 130 μm/min flow rate reported at 30 Hz [12]. A PVDF-TrFE membrane actuated by a PVDF-TrFE film was reported as an actuator-membrane device by Xu et al. [18]. Information in detail about these studies is given in Table 1.1.

***Rotary***

Rotary-type micropumps are inspired from the macro-scale pumps, and pumping action is usually generated by micro-gears that are fabricated using microfabrication methods. These gears add momentum to the fluid through rotational movement. Primary advantage of rotary-type micropumps is the ability of pumping viscous fluids at tens of microliters per minute. However, their fabrication processes are very challenging and it is difficult to achieve desired gap between gears and housing that would cause back flow [19]. Another drawback is that they need an external or internal motor to rotate the gears which increases the size of the pump.

***Peristaltic***

The working principles of peristaltic pumps are based on the peristaltic motion of serial pumping chambers. This motion squeezes the working fluid from one point to another. These types of micropumps usually have at least three pump chambers and three membranes attached with actuators. These actuator-membrane couples are driven at

different frequencies in order to squeeze the flow in desired direction [20]. Since the flow is directed by the serial actuators, peristaltic micropumps do not need an active or passive valve. Therefore, they do not need high pressures inside the channel to operate the valves. Although they are structurally simplistic since they do not require valves, reverse leakage can be an important problem for peristaltic pumps [3]. However, the major disadvantage of the peristaltic micropumps is that the multiple actuators require complex electronics to drive these pumps [2].

### 1.5.2. Non-mechanical Micropumps

Non-mechanical micropumps work based on energy conversion of non-mechanical energy to kinetic which gives momentum to the working fluid. This principle can only be used at microscale [7]. Design of these types of micropumps is simpler than that of the mechanical micropumps since they do not have moving parts. The most common types of non-mechanical micropumps are briefly introduced in the following subsections.

#### *Capillary*

Capillary micropumps work based on surface tension. Since the flow does not require any external power and only driven by surface tension, they can easily be miniaturized and integrated to many microfluidic devices, such as on-site diagnostic applications [21]. However, controlling of this type of micropumps is not precise.

#### *Electrohydrodynamic (EHD)*

The electrohydrodynamic micropumps work based on charges that are induced in the fluid by electrodes. These electrodes are placed next to each other on one side of the chamber and called as emitter and collector. The fluid flow is directed by interaction of

electric fields with the charges induced in the fluid [7]. Although EHD-type micropumps require relatively low driving voltage (40–60V), a complicated geometry is needed to ensure sufficient degree of electro-chemical reactions, and the working fluid must be low conductive and dielectric. [8].

***Bubble-type***

Bubble-type micropumps consist of a chamber, resistive heaters, and fluid directing elements contrary to other non-mechanical pumps. As a result of heated fluid, an air bubble occurs inside the chamber. This bubble expands or collapses proportional to the heat. When the bubble expands, the pressure inside the channel increases and fluid is transported from the chamber to outlet. When the bubble collapses, the pressure decreases, thus the fluid flows from inlet to the chamber. Tsai and Lin developed a bubble-type micropump with diffuser / nozzle elements in 2002 [22]. They reported 5 μm/min flow rate when the driving pulse is 250 Hz at 10% duty cycle.

***Electrochemical***

Electrochemical micropumps work very similar to bubble micropumps. They consist of a bubble reservoir filled with redox electrolyte solution, electrodes and inlet-outlet reservoirs. The electrochemical reaction during electrolysis generates bubbles that provide the driving force to dispense the liquid. Although their designs are simple, control of the bubbles is not easy. Utilized bubble might collapse and become water leading to unreliable release of drug [7].

***Electrowetting (EW)***

Electrowetting (EW)-type micropumps work based on exerted electrostatic to control the surface tension between two layers of material. The fluid is transported using this surface tension. The layers could be either liquid/liquid or solid/liquid as long as they are totally two-phased. EW can be operated in continuous or digital approaches. Continuous EW is usually applied to modify the surface tension between two immiscible liquids such as electrolyte and liquid-phased metal [8].

***Magnetohydrodynamic (MHD)***

The magnetohydrodynamic theory is based on the interaction between the electrically conductive fluid and the magnetic field. A MHD pump consists of two walls bounded by electrodes in order to generate the electric field and the other two walls perpendicular to electrodes are bonded by permanent magnets of opposite polarity to generate the magnetic field. In order to generate fluid flow, the working fluid must be electrically conductive. It is reported that the fluid should have a conductivity of 1 s/m or higher [7]. The most common drawback of this type of micropump is bubbles that are generated due to ionization.

***Evaporation***

Evaporation-type micropumps consist of a porous membrane and a gas space that contains a sorption agent. The working principle of the evaporation-type micropump is similar to the xylem food transport system in trees. No external energy or moving parts are needed for evaporation-type micropumps and fabrication costs are relatively low. This type of micropumps are very useful for continuous glucose monitoring where a dialysis solution is pumped in a continuous mode at small flow rates through

a microfluidic system [7]. On the other hand, they are not suitable for many micropump applications since they only work in suction mode.

### 1.6. Thesis Organization

A fully biocompatible piezoelectrically-activated membrane-type micropump with diffuser / nozzle elements is presented in this thesis. In chapter 2, the background of piezoelectricity, piezoelectric actuator, and diffuser / nozzle elements with literature survey are discussed. In chapter 3, finite element modeling of the micropump and comparison study of commonly used materials for micropumps are presented. In chapter 4, microfabrication of the micropump and diffuser / nozzle devices and detailed information about the challenges and fabrication optimization of PVDF-TrFE thin films are explained. In chapter 5, the experimental setups and results are presented. The major challenges encountered during the experiments are shown as well. Conclusions and intended future works are given in chapter 6.

**Table 1.1 Literature survey of recent micropump studies.**

| | Development, characterization, and theoretical evaluation of electroactive polymer-based micropump diaphragm January-2005 [18] | Piezoelectric Micropump with Nanoliter Per Minute Flow for Drug Delivery Systems September-2010 [14] | An Electromagnetically Actuated All-PDMS Valveless Micropump for Drug Delivery July-2011 [15] | A compact and high flow-rate piezoelectric micropump with a folded vibrator September-2014 [17] | Inkjet printed micropump actuator based on piezoelectric polymers: Device performance and morphology studies September-2014 [12] | Analytical modelling, simulations and experimental studies of a PZT actuated planar valveless PDMS micropump December-2014 [16] |
|---|---|---|---|---|---|---|
| **Author(s)** | Tian-Bing Xu *et al.* | J. Johari *et al.* | Y. Zhou *et al.* | X.Y. Wang *et al.* | Oliver Pabst *et al.* | S. Singh *et al.* |
| **Membrane Material** | PVDF-TrFE | Silicon (100) | PDMS (10:1) | Rubber | PET | PDMS (5:1) |
| **Actuator Material** | PVDF-TrFE | PZT | Micro Magnet (NdFeB) | PZT-4 sheets & Folded Vibrator | PVDF-TrFE | PZT-5A |
| **Membrane Dimensions** | Φ = 1mm / t = 10µm | 12 x12 x 0.1(mm) | t ≈ 300 µm | 20 x 20 x 0.3 (mm) | Φ = 15mm / t = 125µm | Φ = 14mm / t = 150µm |
| **Actuator Dimensions** | Φ ≈2mm / t=10µm | 5 x 10 x 0.2 (mm) | 3 X 3 X 0,5 (mm) | 20 x 20 x 13.5 (mm) | Φ ≈ 10mm / t=9µm | Φ = 11mm/ t = 130µm |
| **Channel Height** | 400 µm | 100µm | 450µm | N/R | 500 µm | 260 µm |
| **Body Material** | Si (100) + $SiO_2$ + $Si_3N_4$ | Silicon (100) | PDMS (5:1) | PDMS & PMMA | Aluminum Alloy (milled) | PDMS (5:1) |
| **Device Dimension** | Φ ~4mm | 14 x 14 x 2 (mm) | 20 x 12 x 3.5 (mm) | 20 x 20 x 28 (mm) | ~250 x 20 x 4 (mm) | ~20 x 10 x 3 (mm) |
| **Operating Voltage** | 80 V/µm | 16 V | N/R | 120V | 700-900V | 30V |
| **Flow Rate** | 550µL/min @1000Hz | 4.98 nL/min @673Hz | 319.6µL/min | 118 ml/min @ 361 Hz | 130 µL/min @30Hz | 20 µL/min @200Hz |
| **Max Back Pressure** | N/A (Not applicable) | N/R (Not reported) | 950 Pa | 22.5 KPa | 56 Pa | 220 Pa |
| **Valve Type** | N/A | Nozzle-Diffuser | Nozzle-Diffuser | Check-Valve | Nozzle-Diffuser | Nozzle-Diffuser |
| **Valve Properties** | N/A | W=200µm , L=650µm, θ=54.7 | W=100µm, L=1600µm, θ=10 | N/R | N/R | W=100µm, L=1500µm, θ=10 |
| **Biocompatibility** | Yes | No | Yes | No | Yes | No |
| **Physics** | Piezoelectrically activated | Piezoelectrically activated | Electromagnetically activated | Piezoelectrically activated | Piezoelectrically activated | Piezoelectrically activated |

## CHAPTER 2. BACKGROUND AND THEORY

### 2.1. Piezoelectricity

Piezoelectric effect was discovered by Jacques and Pierre Curie in 1880. Piezoelectricity is the electric charge that is observed in response to an applied mechanical stress in certain materials such as crystals and ceramics. Likewise, a mechanical strain is generated in response to an applied electric field. Generating an electric charge from a mechanical stress is termed as direct piezoelectric effect while generating a mechanical strain from an applied electric field is termed as reverse piezoelectric effect. Generated electrical charge or mechanical strain from a piezoelectric material is proportional to the amplitude of the applied mechanical stress or electrical field respectively. The illustration of the deformation of a piezoelectric crystal under reverse piezoelectric effect is shown in Figure 2.1.

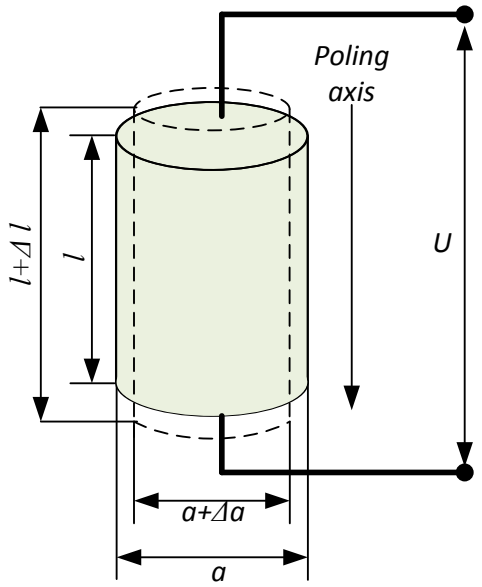


**Figure 2.1: Illustration of the reverse piezoelectric effect. It shows deformation of a piezoelectric material when subjected to an electrical field. The figure adapted from [1].**

The linear equation that governs the piezoelectric effect is given in Eq.8.

$$S = s^E T + dE \quad \text{(Eq.8)}$$

where $S$ is the strain, $s^E$ is the compliance tensor under constant electric field, $T$ is the stress, $d$ is the piezoelectric charge constant tensor, and $E$ is the electric field. If mechanical loads are ignored, this equation becomes;

$$\Delta l = d_{33} U = d_{33} \frac{U}{l} l = d_{33} E l \quad \text{(Eq.9)}$$

and

$$\Delta a = d_{31} U = d_{31} \frac{U}{l} a = d_{31} E a \quad \text{(Eq.10)}$$

where $\Delta l$ is elongation along the poling axis, $l$ is the device length along the poling axis, $U$ is the electrical voltage, $\Delta a$ is elongation perpendicular to the poling axis, and $a$ is the device length perpendicular to the poling axis.

Quartz, $LiTaO_3$, PZT, ZnO, AlN, $MgSi_3$, PVDF, and its copolymer PVDF-TrFE are examples of piezoelectric materials. Piezoelectric films such as ZnO and AlN can be obtained by optimizing the deposition process to form highly oriented films that grow along their c-axis [23]. These properly deposited films exhibit piezoelectricity without any further treatment. However, an additional process called poling is needed for ferroelectric materials such as PVDF-TrFE to modify their spontaneous polarization caused by non-zero dipole moments in their unit crystal cells. The direction of this polarization can be easily modified by applying a strong external electric field as shown in Figure 2.2. The ability to modify the polarization of ferroelectric materials by applying an external voltage eliminates the need to grow a well oriented film which is highly dependent on the environment of the deposition and equipment capacity.

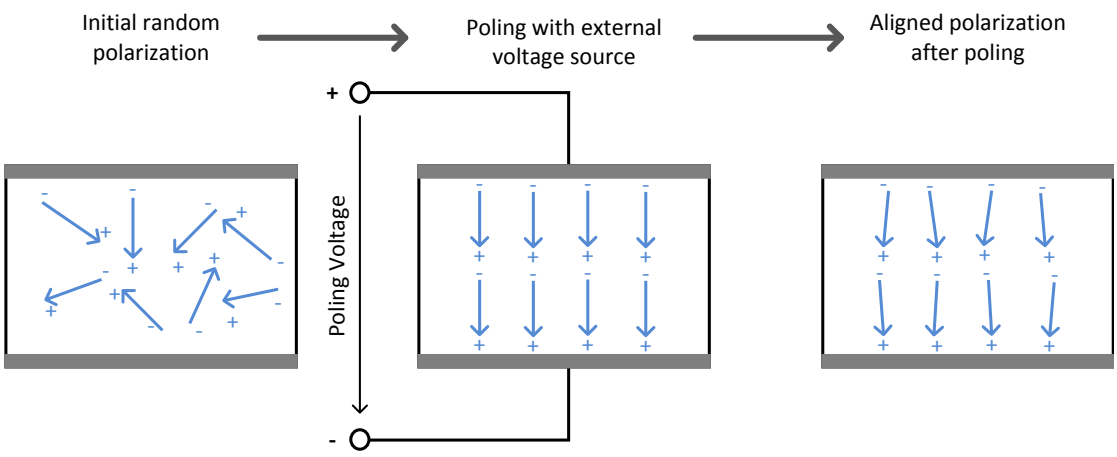


**Figure 2.2: Illustration of the poling process. Spontaneously oriented crystalline domains are aligned by an applied external voltage, and the alignment is conserved after removing the applied voltage.**

## 2.2. Piezoelectrically Activated Valveless Micropump

Piezoelectrically activated pumps consist of a piezoelectric material that is attached to the membrane which seals the pump chamber, and a fluid directing element such as check valves, and diffuser / nozzles. The membrane deformation occurs due to an applied voltage to the piezoelectric actuator. A volume change arises from this deformation as shown in Figure 2.3 and Figure 2.4. When the direction of the electric field is changed, the membrane moves up or down, resulting in volume increasing or decreasing inside the channel, respectively. The increased volume decreases the pressure, resulting in the fluid flowing from inlet to the chamber. Similarly, the fluid flows from the chamber to the outlet when the membrane moves down. These two actions count as one stroke.

A piezoelectric actuator can be fabricated using a piezoelectric disk [16] or piezoelectric sheet [24, 25] that is bonded on top of a membrane, or a piezoelectric material can be directly deposited on top of a membrane by sputtering [26], inkjet-printing [12] or spin coating.

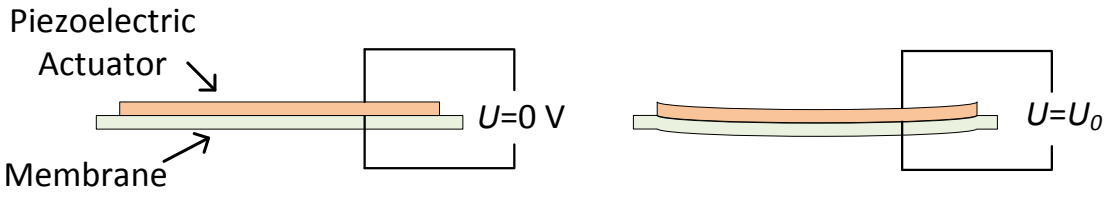


**Figure 2.3: Illustration of the actuator-membrane bending due to an applied voltage to the piezoelectric actuator.**

Piezoelectric micropumps are the most popular micropumps due to their relatively higher displacement in small sizes [5, 11-14, 17, 19, 27, 28]. Most of the proposed piezoelectric actuators are fabricated from PZT due to its much higher displacement compared to other piezoelectric materials such as ZnO, AlN, PVDF, and PVDF-TrFE. However, polymer-based piezoelectric materials attracted a growing interest in recent years due to their easy and cheap fabrication processes, flexibility, and excellent biocompatibility [11-13, 25, 29]. In this thesis, a spin coated thin film PVDF-TrFE is proposed as the actuator and also as the membrane.

Most reported membrane-based micropumps use diffuser / nozzle elements as fluid directing mechanism as shown in Figure 2.4. The first diffuser / nozzle valve was presented by Stemme et al. in 1993 [30] and has been widely studied since then [15, 16, 19, 30-40]. A diffuser has a gradually diverging flow channel while a nozzle has a converging flow channel. They can be designed as conical or flat-walled as shown in Figure 2.5. However, the conical diffusers are 10 to 80 percent longer than the flat-wallet diffuser for the same capacity [1].

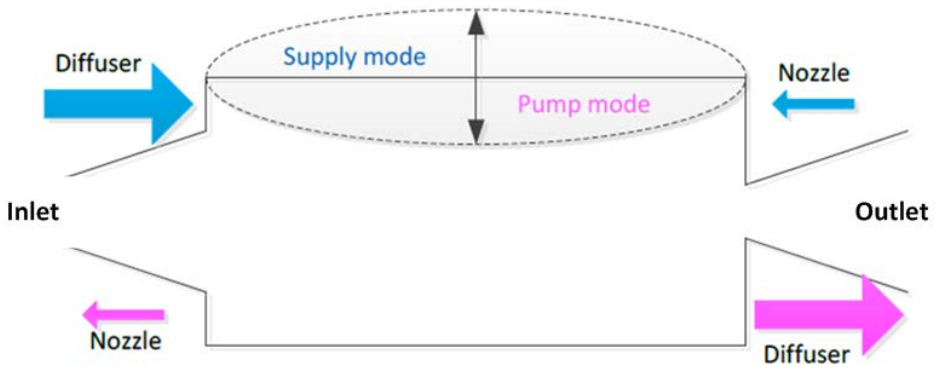


**Figure 2.4: Illustration of the membrane-type micropump with diffuser / nozzle elements. When membrane moves up (supply mode), fluid flows to the chamber mostly from inlet (blue diffuser direction) due to the higher losses at the outlet throat. Similarly, fluid inside the chamber is transferred mostly from the outlet (pink diffuser direction) when the membrane moves down (pump mode).**

Diffuser / nozzle pairs work as flow directing elements based on the pressure drop on two ends of a diffuser. They are extensively preferred to classic active valves or passive check valves due to their simple and low cost fabrication, and absence of wear-fatigue problems since diffuser valves have no moving parts [1]. In addition to these advantages, they also minimize valve clogging problems if beads or cells are going to be used in the fluid. However, the design of diffusers is not straightforward, and small changes on the geometry can have major effects on diffuser performance.

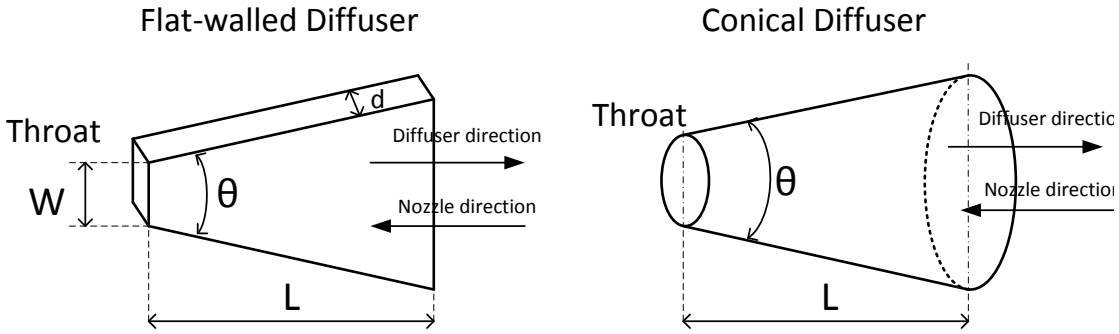


**Figure 2.5: Illustration of flat-walled and conical diffuser elements with important design parameters.**

The pressure drop at the two ends of diffuser is usually given as the loss coefficient, *K,* which is related to the pressure drop, $\Delta p$. $\Delta p$ can be calculated from the fluid density, $\rho$, the mean velocity in the throat, $\bar{v}_{throat}$, and pressure loss coefficient, $\xi$.

$$\Delta p = K\frac{1}{2}\rho\bar{v}_{exit}^2 = \xi\frac{1}{2}\rho\bar{v}_{throat}^2 \quad \text{(Eq.11)}$$

The relation between $K$ and $\xi$ can be calculated from the area ratio of the two ends of a diffuser.

$$\xi = K\left(\frac{A_{throat}}{A_{exit}}\right)^2 \quad \text{(Eq.12)}$$

And the diffuser element efficiency can be defined as

$$\eta = \left(\frac{\xi_{negative}}{\xi_{positive}}\right) \quad \text{(Eq.13)}$$

where $\xi_{negative}$ is the total loss coefficient through converging-wall direction, and $\xi_{positive}$ is the total loss coefficient though diverging-wall direction.

A diffuser performance mainly depends on the diverging angle $\theta$, the area ratio of the outlet to inlet ($A_{out}$ / $A_{in}$), the slenderness, which is diffuser length / inlet width (L/W), and Reynolds number [34]. In order to achieve the best pump performance, the diffuser element has to be designed for highest flow direction capability. Majority of information available in literature is for macro-scaled devices. However, they have been widely used for micro-scaled devices as well. For example, a stability map for diffusers, which was drawn with angle and slenderness variations, has been widely used in order to estimate the flow directing capability. This map can be found from the reference book [10].

Many groups have studied new geometries to reduce diffuser losses and reported their effects on pump efficiency, back pressure and flow rates [30, 31, 34, 35, 38].

Wang et al. studied different rounded inlets to reduce the entrance loses [34]. Yang et al. reported the effects of two-fin and obstacle structures in the diffuser element to increase the pressure drop [31]. Chen et al. fabricated a curved diffuser profile to reduce the back flow inside the diffusers [33]. Olsson et al. fabricated and experimentally tested silicone micro-machined diffusers and reported that the pump efficiency, and thereby the diffuser efficiency, increases with diffuser length, but the effect of the diverging angle was not linear for methanol as working fluid while the efficiency decreases with the diffuser length and the diverging angle for water [36]. Jiang et al. presented a silicone diffuser / nozzle element and reported that the diffuser efficiency increases with the decreasing angle for high Reynolds number ranges (~2000) while it is opposite for low Reynolds number ranges (~50) [37]. Nakamachi et al. studied PDMS diffuser / nozzle elements, and reported that the efficiency increases with increasing angle, and it changes nonlinearly with the diffuser length when water is used as working fluid [11]. All these references show that the diffuser performance is highly affected by working fluid and diffuser material interface besides its geometry. Although, there is sufficient information in the literature about effects of the diffuser geometries on micropumps, effects of the working fluid-microchannel material coupling on diffuser valves has not been studied directly. However, this type of work with commonly used materials can help to determine the desired simple diffuser geometry in the first place. Therefore, we have fabricated and tested different PDMS microdiffusers with deionized water (DIW) to find an optimal geometry for our application. More details about the test diffusers are discussed in the next chapters.

# CHAPTER 3. MODELING AND FEM SIMULATIONS

Finite element analysis is useful in calculating physical phenomena and designing complex devices. The proposed membrane-actuator device was modeled and analyzed with COMSOL Multiphysics finite element modeling (FEM) software. Common piezoelectric materials such as PZT, ZnO, and PVDF-TrFE were studied as actuator materials and their results were compared. Then, the common membrane materials were studied with the selected actuator from the aforementioned study, and the results were compared. Finally, geometry studies (diameter and thickness) were made with the selected actuator and membrane materials. Following subsections discuss the FEM results and optimized membrane-actuator structure.

## 3.1. Comparison of Actuator Materials

Most of the piezoelectric micropumps are actuated by PZT due to its strong piezoelectric properties, which results in high displacement and fast response. However, PZT is not CMOS compatible due to its high temperature thermal annealing requirement for crystallization. The high temperature thermal annealing problem can be resolved by using bulk PZT ceramic disks or sheets, but this solution brings an extra bonding step and makes the device sizes larger. Additionally, PZT ceramics are not biocompatible since they contain lead. Biocompatibility is the most important parameter in micropumps if they are going to be used for biomedical applications. Several methods have been reported to make PZT ceramics biocompatible. For example, Sakai et al. reported that thin film titanium covered PZT shows good biocompatibility [41]. However, these solutions bring additional fabrication steps, and extra cost.

ZnO is another common piezoelectric material that has been studied for micropump actuations. ZnO is a CMOS compatible material unlike PZT. It can be directly sputtered on substrates, and properly deposited ZnO shows piezoelectric behavior without any further treatment such as temperature annealing or mechanical stretching. However, proper deposition of ZnO is very challenging and costly.

In addition to these materials, polymer-based piezoelectric materials have become popular and several polymer-based micropump actuators have been reported in the last decade. PVDF and its copolymer PVDF-TrFE are the most common ones and show similar piezoelectric properties. They both can be easily deposited by spin coating. However, thermal annealing is needed between Curie and melting temperatures in order to crystallize coated PVDF-TrFE into piezoelectric $\beta$-phase, while mechanical stretching is required for coated PVDF [42]. Thermal annealing is simpler and more suitable than stretching for a microfabricated device, therefore PVDF-TrFE is preferred over PVDF in this study. The annealing temperature is lower than 160 °C for a copolymer with 70-80% VDF ratio [43]. In addition to its simple fabrication, being CMOS compatible, and biocompatible, it is also softer and more flexible than previously mentioned piezoelectric actuators. This property is very useful for micropump applications since flexibility of the polymer-based actuators allows generating higher strain.

An FEM simulation study was performed in order to compare performances of these materials as actuator for the membrane-type micropumps. A simple axial symmetric 2D geometry was used to save computational time since the motion of the membrane is in the vertical direction and both membrane and actuator are cylindrical. The 2D model and boundary conditions are shown in Figure 3.1. The membrane material chosen for this

study was poly-methyl-methacrylate (PMMA), since it is one of the most widely used membrane material.

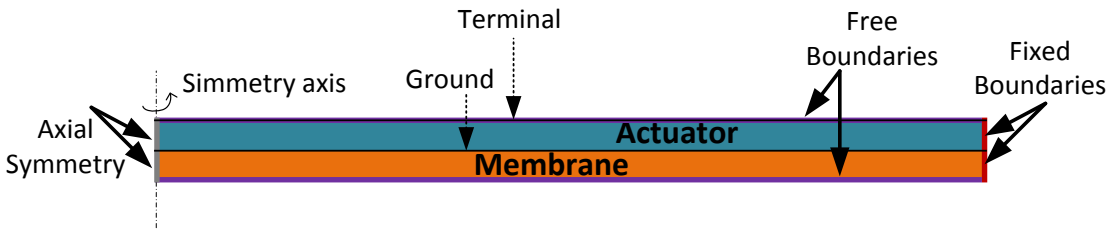


**Figure 3.1: The schematic of the simulated 2D model and its boundary conditions. The diameter is 1000 µm, and the thickness of both the actuator and the membrane is 2 µm for all material comparison studies.**

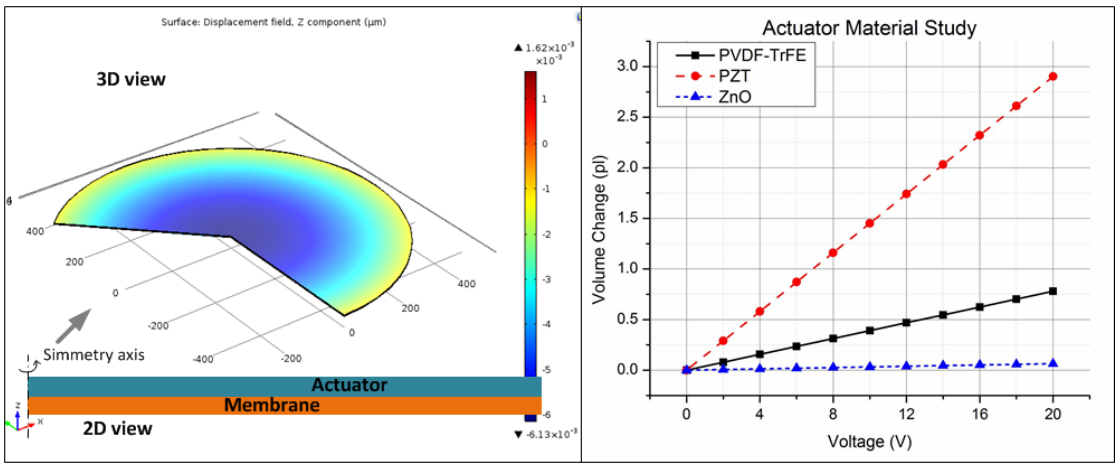


**Figure 3.2: FEM simulation results for different actuator materials. Membrane and actuator thicknesses were fixed as 2 µm and device diameter was set as 1000 µm. The 3D figure shows the displacement result of PZT-PMMA actuator-membrane structure @20 V. The highest deformation, therefore the highest volume change was obtained from PZT, and followed by PVDF-TrFE and ZnO.**

As seen from the results, PZT showed the best performance, and PVDF-TrFE showed relatively higher deformation than ZnO. However, PVDF-TrFE was chosen over PZT for this study because of biocompatibility and CMOS compatibility concerns.

**Table 3.1 Material parameters used in FEM study for comparison of actuator materials.**

| Property | Value | | |
|---|---|---|---|
| | **PZT-(5A)** | **PVDF-TrFE** | **ZnO** |
| **Density ($kg/m^3$)** | 7750 | 1760 | 5680 |
| **Relative Permittivity** | {1730, 1730, 1700} | {7.40, 7.95, 7.90} | {9.16, 9.16, 12.64} |
| **Compliance matrix ($x10^{-11}$) (1/Pa)** | $\begin{bmatrix} 1.64 & -0.72 & 0 & 4.75 & 0 & 0 & 0 \\ -0.57 & -0.72 & 0 & 0 & 0 & 0 & 0 \\ 1.64 & 1.88 & 0 & 0 & 4.75 & 0 & 4.43 \end{bmatrix}$ | $\begin{bmatrix} 33.2 & -8.9 & 0 & 940 & 0 & 0 & 0 \\ -14.4 & -8.6 & 0 & 0 & 0 & 0 & 0 \\ 32.4 & 30 & 0 & 0 & 963 & 0 & 144 \end{bmatrix}$ | $\begin{bmatrix} 0.79 & -0.22 & 0 & 2.36 & 0 & 0 & 0 \\ -0.34 & -0.22 & 0 & 0 & 0 & 0 & 0 \\ 0.79 & 0.69 & 0 & 0 & 2.36 & 0 & 2.26 \end{bmatrix}$ |
| **Coupling matrix ($x10^{-12}$) (C/N)** | $\begin{bmatrix} 0 & 0 & 0 & 0 & 584 & 0 \\ 0 & 0 & 0 & 584 & 0 & 0 \\ -171 & -171 & -374 & 0 & 0 & 0 \end{bmatrix}$ | $\begin{bmatrix} 0 & 0 & 0 & 0 & 36.3 & 0 \\ 0 & 0 & 0 & -40.6 & 0 & 0 \\ 10.7 & 10.1 & -33.5 & 0 & 0 & 0 \end{bmatrix}$ | $\begin{bmatrix} 0 & 0 & 0 & 0 & -11.34 & 0 \\ 0 & 0 & 0 & -11.34 & 0 & 0 \\ -5.43 & -5.43 & -11.67 & 0 & 0 & 0 \end{bmatrix}$ |

## 3.2. Comparison of Membrane Materials

Polydimethylsiloxane (PDMS) and poly-methyl-methacrylate (PMMA) are the most common membrane materials in microfluidic applications because of their flexibility, low cost fabrication, biocompatibility, and transparency. The selected actuator material, PVDF-TrFE, is also a polymer and biocompatible making it promising for membrane structure as well. Besides the flexible and transparent polymers, using thin film $SiO_2$ as membrane material is also common due to their easy fabrication. However, in contrast with the polymer membranes, $SiO_2$ become very fragile once it is suspended - hence cannot handle high strain.

A comparison FEM study was performed using these materials with the selected actuator material (PVDF-TrFE) from the previous study. The thicknesses and the diameters of the membrane and the actuator structures are fixed as 2μm and 1000 μm, respectively. Results are shown in Figure 3.3. Material properties used in this study are giving in Table 3.2.

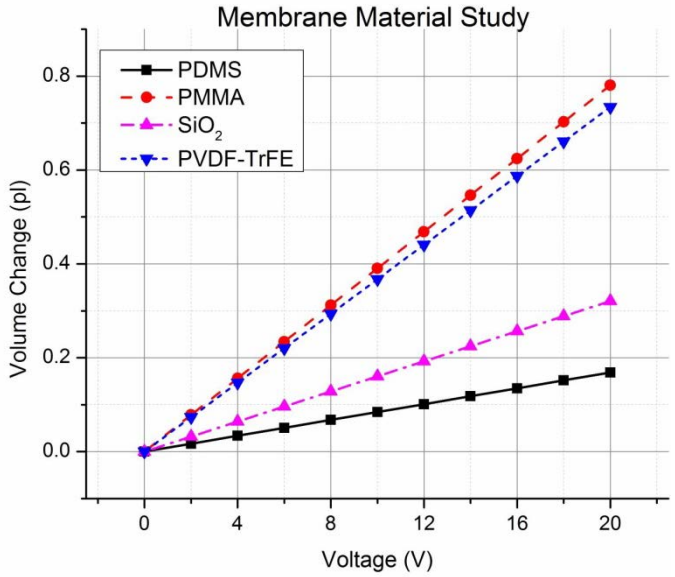


**Figure 3.3: FEM simulation results for membrane material optimization. Membrane and actuator thicknesses were fixed as 2 µm and device diameter set as 1000 µm. PVDF-TrFE and PMMA showed the same pattern while PDMS showed the lowest volume change.**

PVDF-TrFE and PMMA showed the highest volume change which is around 0.8 pL/stroke at 20 V, followed by $SiO_2$ with 0.3pL/stroke while PDMS showed the smallest volume change which is around 0.18 pL/stroke at 20 V. PVDF-TrFE was chosen over PMMA since it can be easily fabricated on the substrate using traditional fabrication methods.

**Table 3.2 Material parameters used in FEM study for comparison of membrane materials.**

| Property | Value | | | |
|---|---|---|---|---|
| | PDMS | PMMA | PVDF-TrFE | $SiO_2$ |
| Density ($kg/m^3$) | 970 | 1190 | 1760 | 2200 |
| Young's modulus (Pa) | 750 | $3x10^9$ | $3.8x10^9$ | $70x10^9$ |
| Poisson's ratio | 0.49 | 0.4 | 0.34 | 0.17 |

We can conclude from these studies that PVDF-TrFE showed the most promising results as both actuator and membrane material. Further FEM studies for optimizing the final device geometry were made from PVDF-TrFE / PVDF-TrFE actuator-membrane pair. In addition to this novel structure, $Si_3N_4 + SiO_2$ membrane structure was also studied, due to our team's understanding and experience on piezoelectric energy harvesters, which are made using PVDF-TrFE on top of $Si+Si_3N_4$ (low stress)$+SiO_2$ substrate [42].

### 3.3. Electrode Architecture Study

The positive effect of clamped electrodes on PZT for an energy harvester was reported by Kim et al. [44]. A similar electrode structure study as shown in Figure 3.4 was made using FEM software for actuation of piezoelectric material. A nested electrode pair structure was used for bottom and top electrodes. Each top and bottom electrode pairs were poled oppositely, and the same electric field is applied to each pair. The obtained displacement results were surprisingly higher than the previous study (undivided electrode structure). The maximum displacement was obtained when $D_{inner} = 0.63D_{total}$, and the maximum volume change was obtained when $D_{inner} = 0.7D_{total}$. Therefore, the electrode architecture was modeled as $D_{inner} = 0.7D_{total}$. The following simulations were performed using the nested electrode structure.

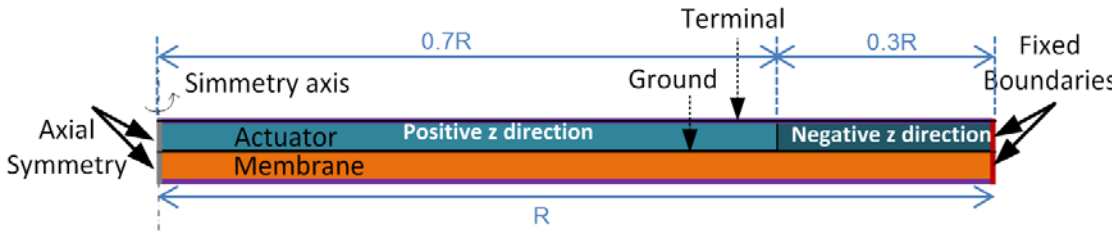


**Figure 3.4: Schematic and boundary conditions of nested electrode structure.**

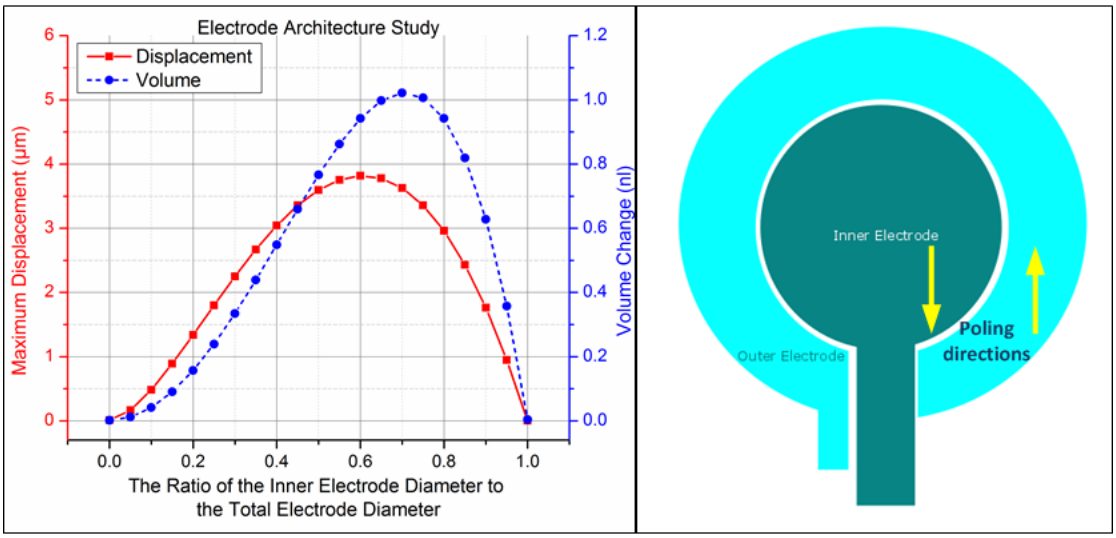


**Figure 3.5: The figure shows the FEM results for effects of the inner electrode diameter and the nested electrode structure. Results are taken from 1000 µm total diameter fully PVDF-TrFE actuator-membrane model at 20 V. The results showed the electrode structure highly effects the deformation. Volume change was approximately two order of magnitude higher than the previous study which has an undivided electrode structure (pL→ nL).**

### 3.4. Geometry Optimization of the Micropump with the Selected Materials

Previous FEM studies showed that using PVDF-TrFE as both the actuator and membrane is very promising. In addition to this, the nested electrode structure showed great improvement on deformation. However, it is important to account for the residual stress of deposited thin films since it can have a profound effect on the stiffness of the membrane structure. The residual stress can be modeled in the simulations using 'Thermal Expansion' in COMSOL, and the residual stress parameters were used in this study are given in Table 3.3. The residual stress parameters of $Si_3N_4$ and $SiO_2$ were obtained from the manufacturer, while the value for PVDF-TrFE (7MPa) was assumed based on the available data from literature.

**Table 3.3 Residual stress values used in the simulations.**

| | PVDF-TrFE | $Si_3N_4$ | $SiO_2$ |
|---|---|---|---|
| **Residual Stress** | 7 MPa | 250 MPa | -400 MPa |

As mentioned before, our group has previously fabricated successful piezoelectric harvesters on $Si_3N_4 + SiO_2$ structural layers. Therefore, a comparative study was performed using PVDF-TrFE and $Si_3N_4 + SiO_2$ as membrane materials. The effects of the actuator thickness and diameter of the membrane on maximum displacement and volume change were studied for both cases. Additionally, a voltage-displacement and also volume change study was made for the finalized structure.

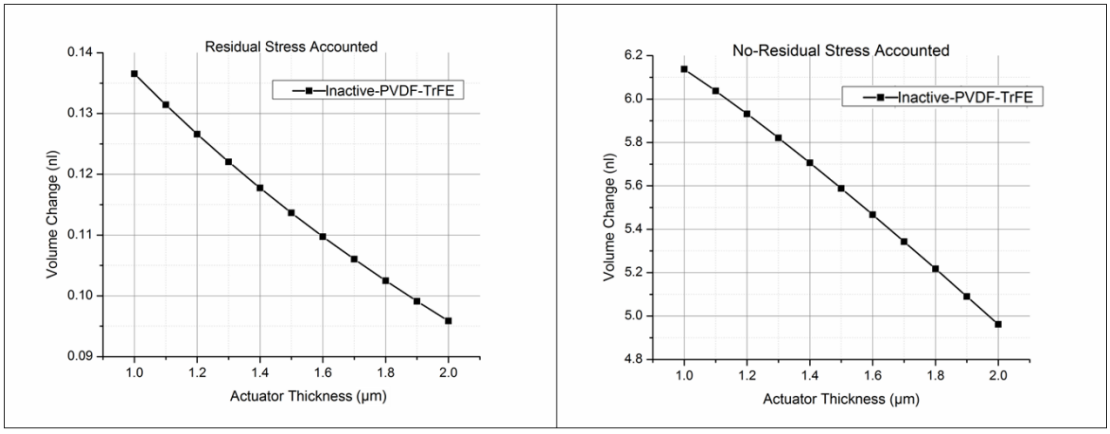


**Figure 3.6: Actuator thickness vs maximum volume change studies for active-inactive (actuator-membrane) PVDF-TrFE. (Study parameters: PVDF-TrFE membrane thickness is 2 μm, and actuation voltage is 20 V.)**

As shown in Figure 3.6, volume change decreases with increasing PVDF-TrFE actuator thickness. Although this result indicates that thinner film provide higher volume change, we purposely coated 1.5 μm thick PVDF-TrFE for the actuator to account for losses during the RIE process. On the other hand, a relatively thick PDVF-TrFE layer (2 μm) was selected for the membrane structure. The main reason for this was to

compensate for over-etching during DRIE process since the membrane releasing process was planned to be carried out using DRIE, and no information was available on the selectivity between silicon and PVDF-TrFE in literature.

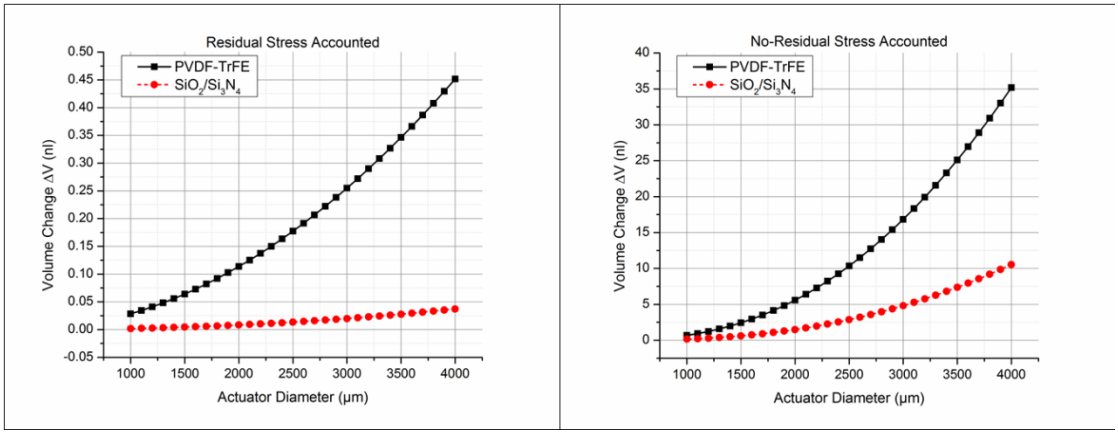


**Figure 3.7: Actuator diameter vs maximum volume change studies for PVDF-TrFE actuator on both PVDF-TrFE and $Si_3N_4$ + $SiO_2$ membranes. (Study parameters: actuator thickness is 1.5 µm, PVDF-TrFE membrane thickness is 2 µm, and actuation voltage is 20 V.)**

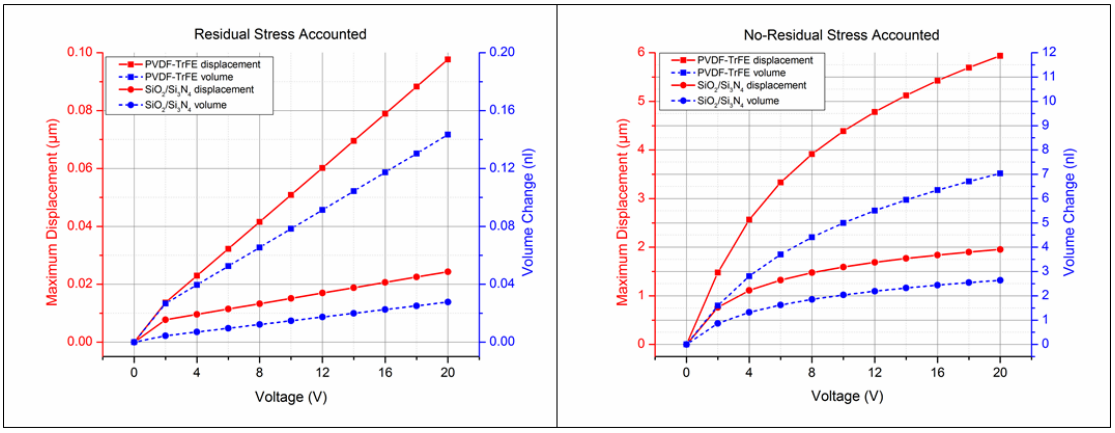


**Figure 3.8: Voltage vs maximum displacement (red), and maximum volume change (blue) studies for PVDF-TrFE actuator on both PVDF-TrFE and $Si_3N_4$ + $SiO_2$ membranes. When the residual stress was accounted for, the output reduces significantly. (Study parameters: actuator thickness is 1.5 µm, PVDF-TrFE membrane thickness is 2 µm, and device diameter is 2000 µm.)**

In conclusion, FEM studies showed that PVDF-TrFE actuator gives higher deformation than the other biocompatible piezoelectric material-ZnO, but lower than PZT. However, the biocompatibility is our priority since the objective of this research is a micropump system that is suitable for biomedical devices. In addition to this, using PVDF-TrFE as the membrane material showed higher displacement when compared to other commonly used membrane materials like PDMS and $SiO_2$.

A 0.1 nL/stroke volume change is obtained from the FEM simulations of 2mm in diameter fully PVDF-TrFE micropump at 12V. Therefore, the designed micropump can generate a flow rate of 60 nL/min at 12V and 5 Hz which is suitable and can be precisely controllable for therapeutic drug delivery systems.

# CHAPTER 4. FABRICATION

Micropump fabrication consists of three major components: membrane, actuator, and microfluidics. Both the membrane and the actuator were fabricated using the same polymer (PVDF-TrFE) on a 4" Si wafer coated with 800 nm-thick low stresses LPCVD silicon nitride ($SiN_x$) and 150 nm-thick PECVD $SiO_2$ layers. PDMS microfluidic channels were fabricated using an SU-8 mold fabricated on a silicon 4" wafer. The microfabrications of the devices were carried out at a class 100 cleanroom. This chapter discusses the designed photomasks, fabrication flows, process steps, challenges and developed solutions**.**

## 4.1. Photomask Design

A total of five masks for the actuator and membrane structures and one mask for microfluidic structures were designed. In addition to the micropump fabrication, another mask was designed for the optimization of diffuser / nozzle elements.

A mask for the circular shape micropump chamber, a mask for both PVDF-TrFE membrane and actuator, a mask for the bottom electrode, a mask for the top electrode, and a mask for the back side membrane release were designed for fabrication of membrane-actuator section. These masks contained 14 different sizes of membranes (1000 μm - 4500 μm) and 44 devices in total. Top and bottom electrodes were designed as inner-outer pairs (nested structure), therefore four pad connections designed for poling purpose.

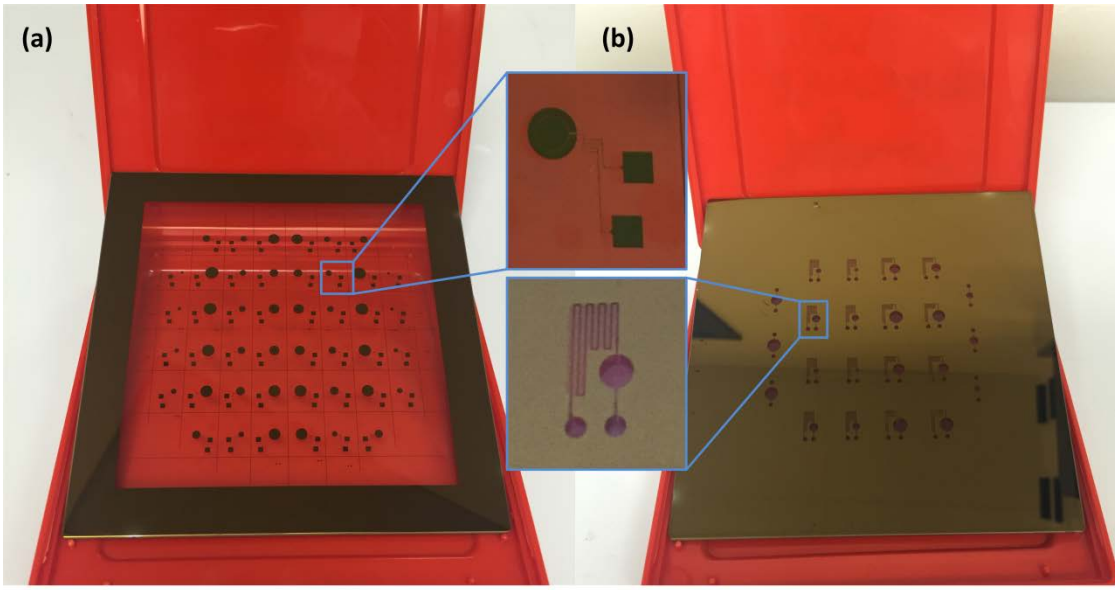


**Figure 4.1: Masks fabricated on 5" soda lime glass. (a) Shows the mask for the bottom electrode of the actuator, (b) mask for the microfluidic channels and diffuser valves.**

Figure 4.1 (a) shows successfully fabricated bottom inner-outer electrode pair mask. Figure 4.1 (b) shows the mask designed to fabricate the SU-8 mold for fabricating the PDMS microchannels and diffuser valves. One chamber size was chosen for two consecutive membrane sizes to save space on the mask. For example, 1350 µm diameter chamber was designed to be used for both 1000 µm and 1250 µm membrane devices. 100 µm margins were used to account for possible fabrication errors and to make the aligning step easier. A total of 8 chamber sizes with two different diverging angles 10° and 15° were designed. Since the micropump was modeled for biomedical applications which need nL / min volumes, spiraled channels with graduated markings were designed to measure flow rate of the micropump quicker and more accurately inside the microchannels. In addition to this, the remaining part of the mask was filled with simple inlet-chamber-outlet type microfluidic channels as a concept for future work. A total of 14 microfluidic channels were designed on this mask.

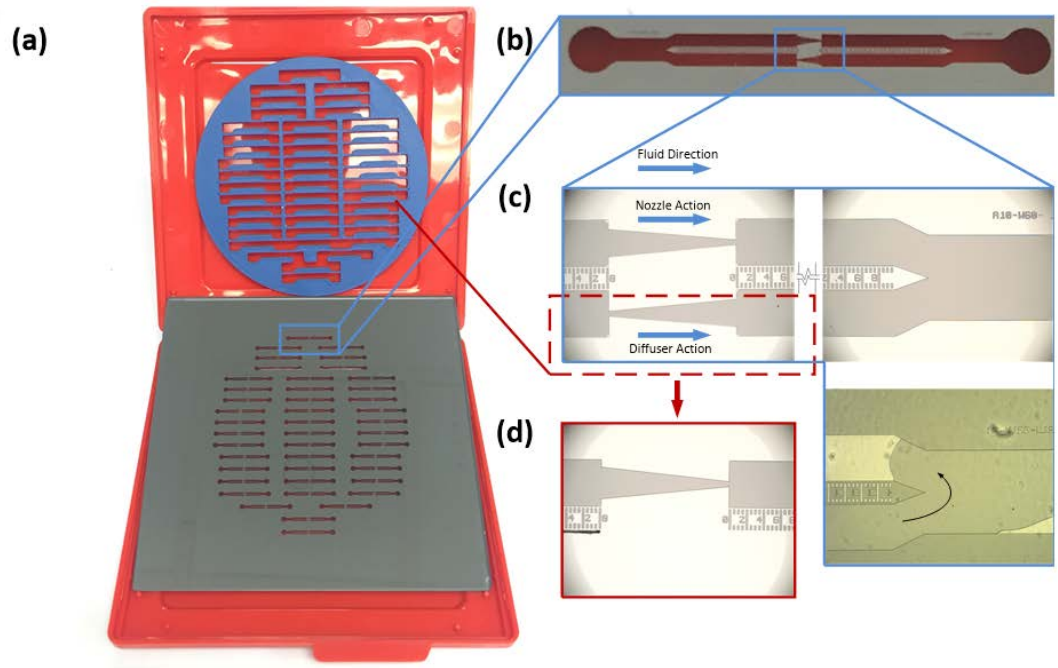


**Figure 4.2: (a) The picture of the diffuser elements test mask and 3D printed shadow mask. (b) A closer look to a printed test structure. (c) Optical microscope images of a fabricated diffuser / nozzle test structure and blocking issue occurred through the nozzle. (d) Fabricated single channel test structure using the same mask and 3D printed custom-made shadow mask.**

Diffuser elements, which directly affect the efficiency of the micropumps, have been studied for decades and improved to reduce the possible losses. However, the data available in literature show that the design of microdiffuser elements is much more complicated than the geometric calculations, and must be unique for the body material and the fluid used. We designed a mask to find an optimal microdiffuser structure for our application which uses a PDMS microfluidic channel bonded on a silicon substrate and DI water used as the working fluid. Diffuser / nozzle elements were drawn next to each other in two parallel microchannels as shown in Figure 4.2 (b-c) to see the diodicity of the valves for both diffuser and nozzle directions. This test setup successfully proved directing capability of all designed diffuser / nozzle structures. However, we could not compare the all diffuser / nozzle pairs due to blocking issue occurred through nozzle

channel by the fluid coming from diffuser channel as shown in Figure 4.2 (c). In order to compare all angle / throat width / length combinations, we decided to do the tests in a single channel by feeding from right or left at a time. For this purpose, a custom-made 3D-printed apparatus was used to block UV on second channels to save time and cost. Figure 4.2 (d) shows an optical image of a single channel diffuser element.

### 4.2. Microfabrication Flow

Fabrication of the microfluidic section of the micropump and diffuser / nozzle test elements were done with 4 steps as shown in Figure 4.3. Microfabrication of the membrane-actuator section was done with 11 main steps as stated in the Figure 4.4. Before the actual microfabrication steps, all substrates were cleaned by acetone, isopropyl alcohol (IPA), and deionized water (DIW), respectively. Detailed information is discussed in the following sections.

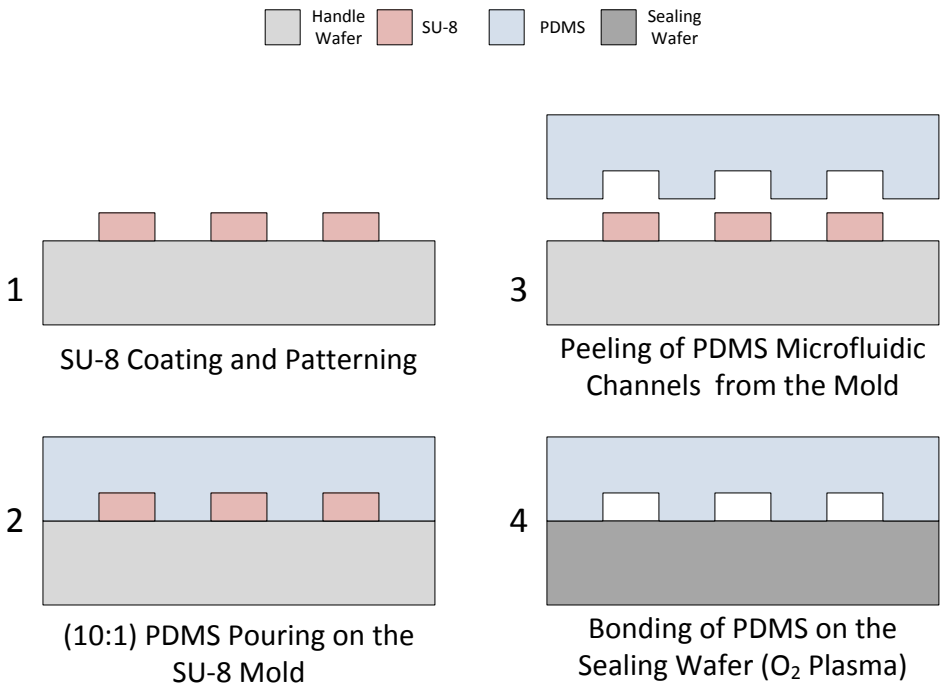


**Figure 4.3: Illustration of the fabrication flow of the diffuser / nozzle test structures and microfluidic section of the micropump.**

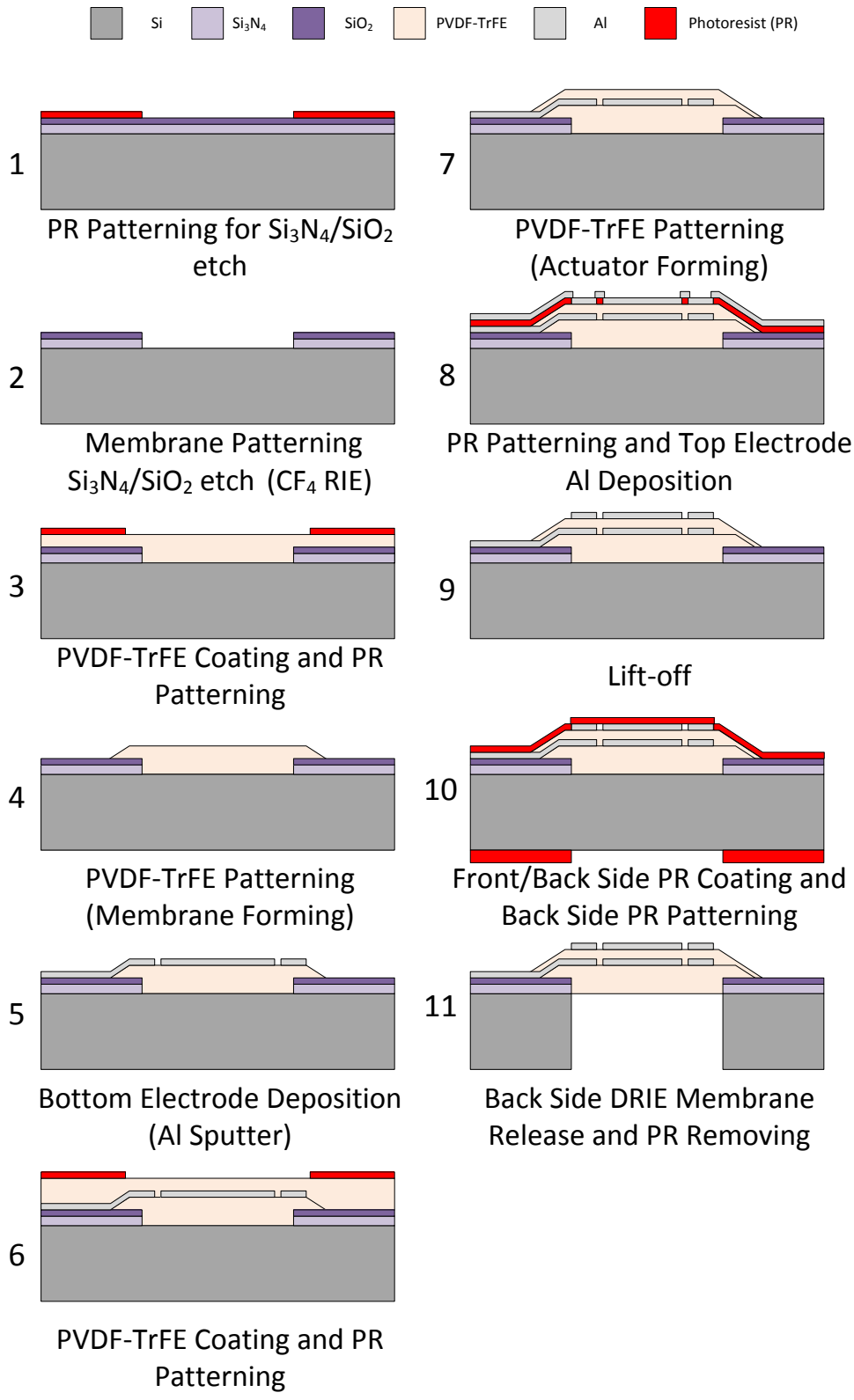


**Figure 4.4: Illustration of the membrane-actuator fabrication process flow.**

### 4.3. Process Steps, Fabrication Challenges, and Developed Solutions

Microfabrication steps of the each section as shown in Figure 4.3 and Figure 4.4, faced difficulties during the fabrication processes, and developed solutions are explained in detail in the following subsections.

#### 4.3.1. Membrane and Actuator Fabrication

First, the piezoelectric polymer polyvinylidene fluoride-trifluoroethylene (PVDF-TrFE) solutions were prepared with 8%, 5%, and 2% weight ratio. PVDF-TrFE powder with 75/25 molar ratio was dissolved in methyl ethyl ketone (MEK) and filtered using quantitative filter papers with pore sizes ranging from 40 µm to 2 µm. Then, the membrane regions were formed by etching 800 nm $Si_3N_4$ and 150 nm $SiO_2$ layers using $CF_4$ / $O_2$-based RIE performed in MARCH-CS1701 model tabletop RIE. The etching process was carried out in 4-5 intermittent steps and the wafer was rotated 90 degrees at every interval due to do spatial non-uniformity of the plasma. Lithography of this layer was carried out with AZ4620-type photoresist coated at 2500 rpm. 950 nm etching was completed in 520 seconds. Process details are given in the Table 4.1and Table 4.2.

Six layers of PVDF-TrFE solution were spin coated in order of, 8-2-5-5-5-2% weight ratio to obtain ~2µm-thick membrane. The reason of this order is discussed in the subsection - *challenges and optimization*. Each spin coating steps was performed at 3500 rpm for 45 seconds and followed by an evaporation step on a hot plate at 100 °C for 10 minutes. The wafer was annealed in an oven at 140 °C for 1 hour after the first 5 spin coating steps, and annealed for 4 hours after the last coating step to improve crystallinity and electrode adhesion. Then, AZ1518-type positive photoresist was coated at 1750 rpm for 30 seconds, patterned and developed in order to etch unwanted PVDF-TrFE regions.

Etching of the film was carried out using $O_2$-based RIE for 330 seconds in total. As previously mentioned, the etching process was carried out in 4-5 intermittent steps. Detailed fabrication information is given in the Table 4.1 and Table 4.2. After etching away unwanted film regions, average thicknesses were measured as 2.2 µm using a TENCOR Alpha-Step 200 profilometer.

**Table 4.1 RIE etch recipes.**

| Etch Process | Power (W) | Pressure (mTorr) | Process gases | Gas flow (sccm) | Etch rate (nm/min) |
|---|---|---|---|---|---|
| $Si_3N_4$ / $SiO_2$ | 170 | 170 | $CF_4/O_2$ | 16/3 | ~110 |
| PVDF-TrFE | 150 | 350 | $O_2$ | 60 | ~350 |

The piezoelectric thin film must be stacked between two electrodes to generate a mechanical strain. Therefore, bottom electrodes were first deposited on top of inactive PVDF-TrFE layer (membrane). Bottom electrode deposition could have done by sputtering and Al etching as shown in the process flow. However, this step was carried out by a lift-off process to examine the possible challenges before moving to the top electrode deposition. The wafer was patterned for lift-off using nLOF 2020-type negative photoresist following by 60 seconds of $O_2$ plasma (descum) to remove the remaining organic residues. Approximately 300 nm of PVDF-TrFE film was etched during the descum step. Therefore, inactive PVDF-TrFE (membrane) thickness was measured as ~1.9 µm. The bottom electrode layer was deposited using an AJA ATC-Orion sputtering system with a 30 minute run for 100 nm-thick layer of Al. The run was carried out in two 15 minutes intervals with a 10 minute cooling break in between the intervals to prevent the PVDF-TrFE film from melting due to overheating. The wafer was dipped in methanol and soaked for an hour after the deposition. Since classic lift-off solvents such as

remover-pg and acetone attack PVDF-TrFE, methanol was used for lift-off process. Then, the photoresist and unwanted metal regions were removed by a 5 minutes sonication step. The soaking and sonicating steps were repeated 3 more times in fresh solutions. The wafer was held upside down using a Teflon holder in order to prevent the removed Al particles from sticking to the surface. After unwanted metals were lifted off, the wafer was removed from the solution, cleaned with DIW, and dried with a nitrogen gun. The second thin layer of PVDF-TrFE (active/actuator layer) was coated in multiple steps using solutions in order of 8-2-8-2-5-2-2% weight ratio to form the actuator. The coated films were annealed and patterned following the same methods used to form the membrane layer. Active PVDF-TrFE layer thickness was measured as 1.5 µm after 60 seconds of $O_2$ plasma descuming that was made for removing the undeveloped thin layer of photoresist and residue before sputtering. The top electrodes were deposited on the second (active) PVDF-TrFE layer, and unwanted metals were lifted off by following the same lift-off procedures used for bottom electrode patterning.

**Table 4.2 Lithography recipes used to form the actuator-membrane devices.**

| Process | Material | Spin Speed (rpm) | Spin Time (sec) | Bake Temperature (°C) | Bake Time (sec) | Exposure Dose (mJ/cm$^2$) | Developer and Duration |
|---|---|---|---|---|---|---|---|
| $Si_3N_4$ / $SiO_2$ Etch | AZ4620 | 2500 | 60 | 110 (Hot Plate) | 210 | 500 | AZ400K 4:1 140 sec |
| PVDF-TrFE Etch | AZ1518 | 1750 | 30 | 100 | 240 | 55 | AZ400K 4:1 105 sec |
| Lift-off | nLOF | 4000 | 45 | 110/110 (PEB) (Hot Plate) | 60/60 | 65 | AZMIF300 90 sec |
| Back Side Si Etch | AZ4620 (2 Layers) | L1-3000 L2-3000 | L1-45 L2-45 | L1 90 (Oven) L2 90 (Oven) | L1-300 L1-1200 | 700 | AZ400K 4:1 240 sec |

The backside microfabrication for membrane release was done using deep reactive ion etching (DRIE). First, a thin layer of AZ1518-type photoresist was coated on the front side of the sample to protect the devices from scratches. Since 500µm-thick silicon was going to be etched, a 16 µm-thick AZ4620-type photoresist was coated and patterned on the back side of the wafer. Step by step process pictures are given in Figure 4.5.

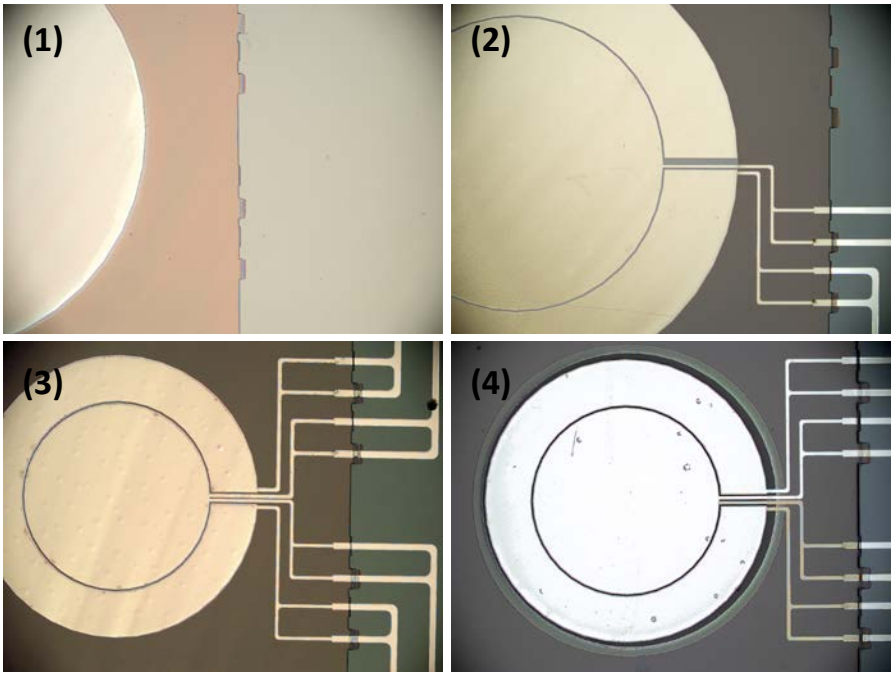


**Figure 4.5: The pictures of (1) a membrane cavity and inactive PVDF-TrFE layer (membrane), (2) a device after bottom electrode deposition, (3) a device after top electrode deposition, and (4) a finalized device after DRIE membrane release.**

After completing the fabrication, the wafer was diced into individual devices using a scriber. The coated photoresists on front and back sides were cleaned using methanol and DIW. Extra attention was needed at this step since the membrane-actuator part of the device was a thin polymer film, and pressured water or nitrogen could easily damage it. The picture and SEM image of the fabricated actuator-membrane devices are shown in Figure 4.6 and Figure 4.7, respectively.

**Figure 4.6: Fabricated and diced membrane-actuator devices.**

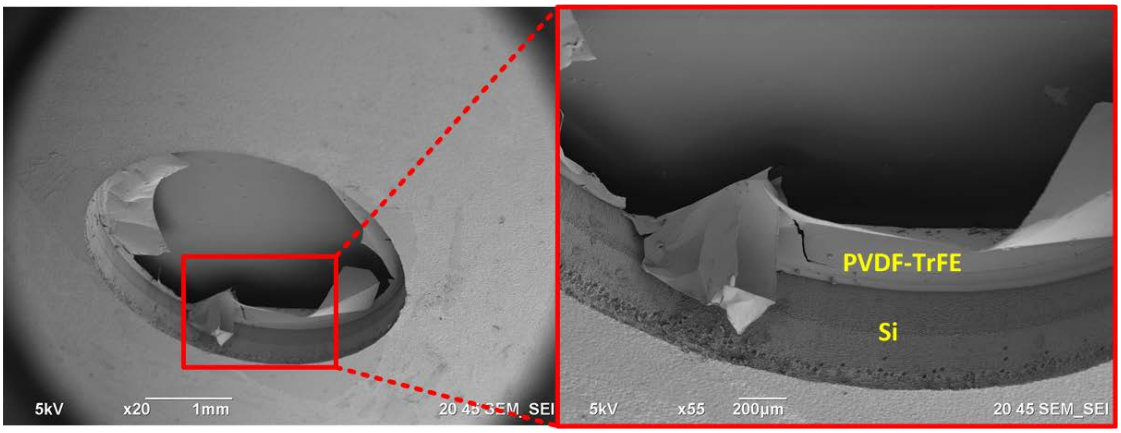


**Figure 4.7: SEM image of an actuator-membrane device.**

## Microfabrication Challenges and Optimization of the Process

Although PVDF-TrFE fabrication requires very simple fabrication steps, unexpected challenges can appear. Since MEK, which was used to prepare the PVDF-TrFE solution, is highly volatile, it is very likely to end up with poor quality and porous films. Several process optimizations were developed in our group during fabrication of PVDF-TrFE

based energy harvesters [42]. In this study, we faced similar and other challenges and had to optimize fabrication process once again.

Viscous solutions such as 8% weight ratio of PVDF-TrFE powder gives non-uniform surfaces with bigger microscopic pores than the ones from 2% weight ratio solution. Photoresist can go under the polymer film through these pores and outgas when it is exposed to UV radiation. This can strip off the film as shown in Figure 4.8. The outgassing issue was also observed even after developing the photoresist because the photoresist that went under the film did not get properly developed. Related pictures are given in Figure 4.9.

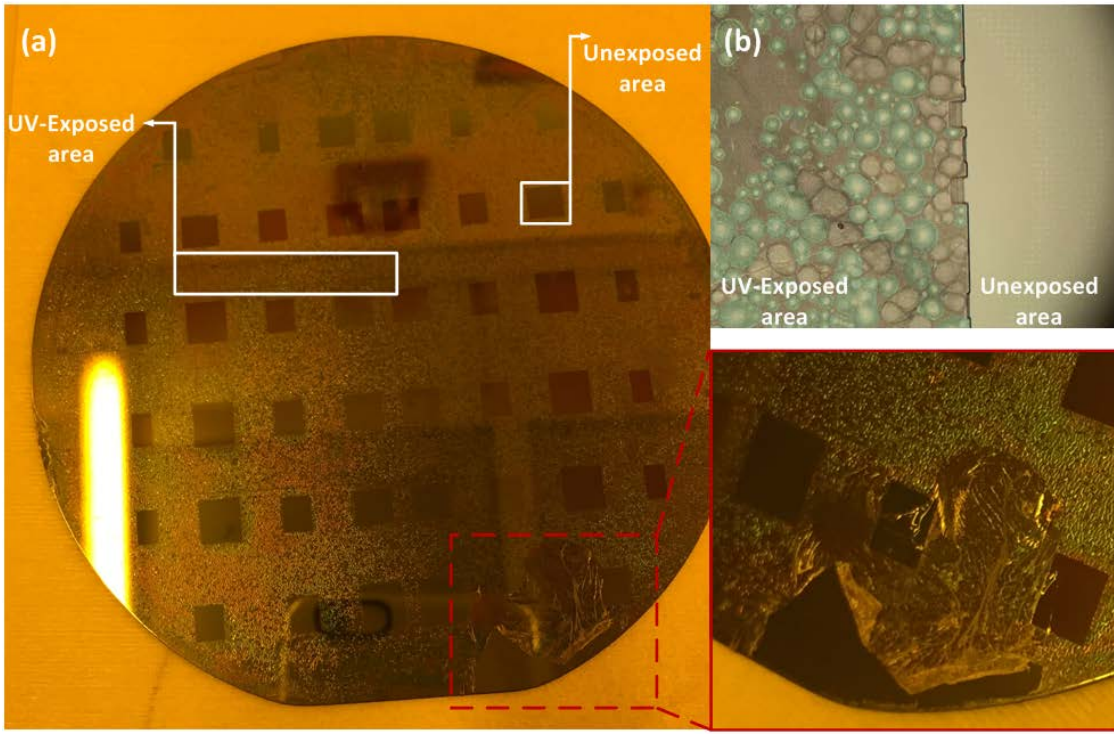


**Figure 4.8: (a) Shows the photoresist coated PVDF-TrFE (4 hours annealed) film after UV exposure. (b) An optical image of the outgassing issue caused by photoresist that went under polymer film from the pores of the film.**

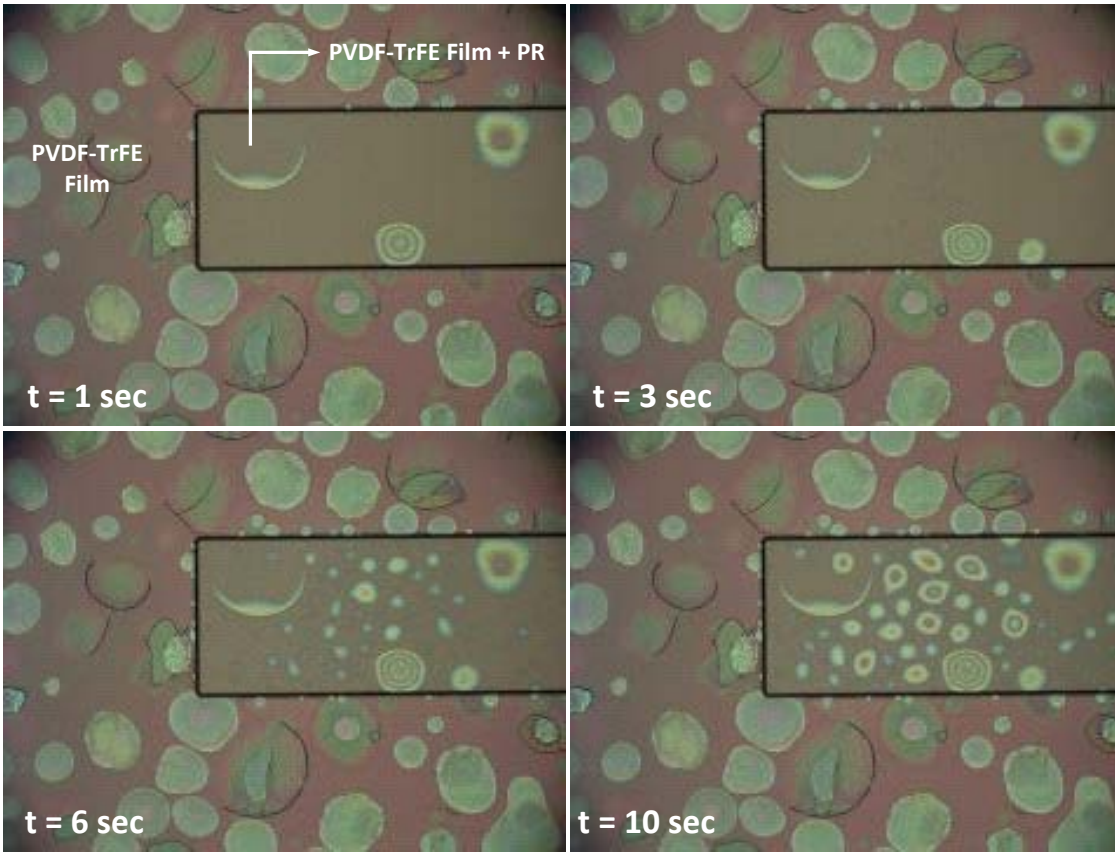


**Figure 4.9: Optical image of the samples after development of photoresist. "t" stands for the time that the sample was subjected to white microscope light and 'PR' stands for photoresist.**

A solution was proposed by Guodong [45] for porous film issue. It was reported that an additional layer of dilute PVDF-TrFE solution coating after each viscous solution can fill the porous and smooth the film surface. Although this solution gives better film quality, it can make the surface worse as shown in Figure 4.10 if some extra precautions will not be taken. Since the dilute solution evaporates quicker than the viscous solution, it causes more pores in the film. In order to slow down evaporation of the solution, high spin speeds and a closed-lid spin coater was used for deposition of the film in early experiments of our group. Though these precautions helped to deposit better quality films, it did not solve the excessive porous film surface completely.

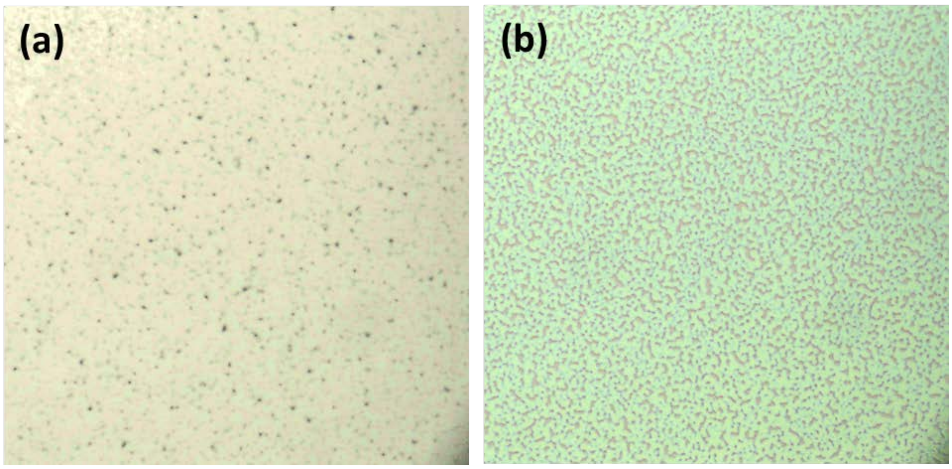


**Figure 4.10: Microscopic image of (a) single step PVDF-TrFE coating using the solution with 8% weight ratio, and (b) after second layer of 2% solution coating on top of 8% coated film.**

Finally, it was found that dominant impact is related to the amount of solution used for spin coating. More solution equals slower evaporation and gives better quality films. However, using dilute solution is still needed for filling the small pores and smoothing the surface. Results after using ample amount of solution are shown in Figure 4.11.

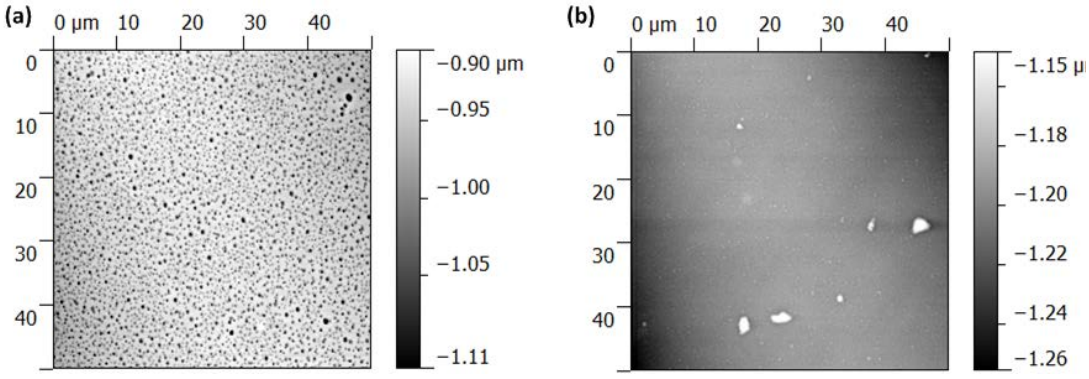


**Figure 4.11: AFM images of (a) the porous film that was caused by quick evaporation (b) coated PVDF-TrFE film after optimization of the fabrication parameters. The images were taken from 2% weight ratio solution coated sample. The big white areas are shown in figure-b are some external particles on the sample.**

### 4.3.2. Microfluidic Channels and Diffuser Valve Fabrication

The diffuser / nozzle test devices and micropump fluidic section were created using soft lithography (molding method). The mold was fabricated with SU8-2025-type photoresist on a silicon wafer using traditional lithography methods as shown in the process flow in Figure 4.3. 26 μm-thick features were obtained from spin speed of 2000 rpm for 60 seconds.

**Diffuser / Nozzle Test Structures**

10:1 ratio PDMS and curing agent (Dow Corning, Sylgard 184 Elastomer) were mixed well, degassed in a vacuum chamber, poured onto the mold, and cured in oven at 50 °C for 150 minutes. Cured PDMS was carefully removed from the mold and inlet-outlet reservoirs were punctured with 1.5 mm diameter biopsy punches. Cured and punctured PDMS device was bonded onto a silicon wafer using RIE $O_2$ plasma for strong bonding to reduce the possible leakages. Although this bonding method gives a quite strong bond, it is only suitable for applications that do not need alignment because the bonding has to be done very quickly after plasma exposure. Since all features were in PDMS for these test devices, no alignment was needed and we could use plasma bonding.

A stream of 20 sccm $O_2$ plasma was applied to the PDMS section under 200 mTorr of pressure and 150 W of power for 20 seconds. Then, the PDMS section was bonded onto the sealing wafer right after the RIE chamber was opened. The sample was then baked in oven at 100 °C for 10 minutes. The fabricated devices are shown in Figure 4.12. In addition to the original two channel test structures, we fabricated single channel devices using the same mask but with a custom-made 3D-printed apparatus as a shadow

mask to block the UV exposure on second channels. The reason for fabricating single channel diffusers is mentioned in the photomask design section.

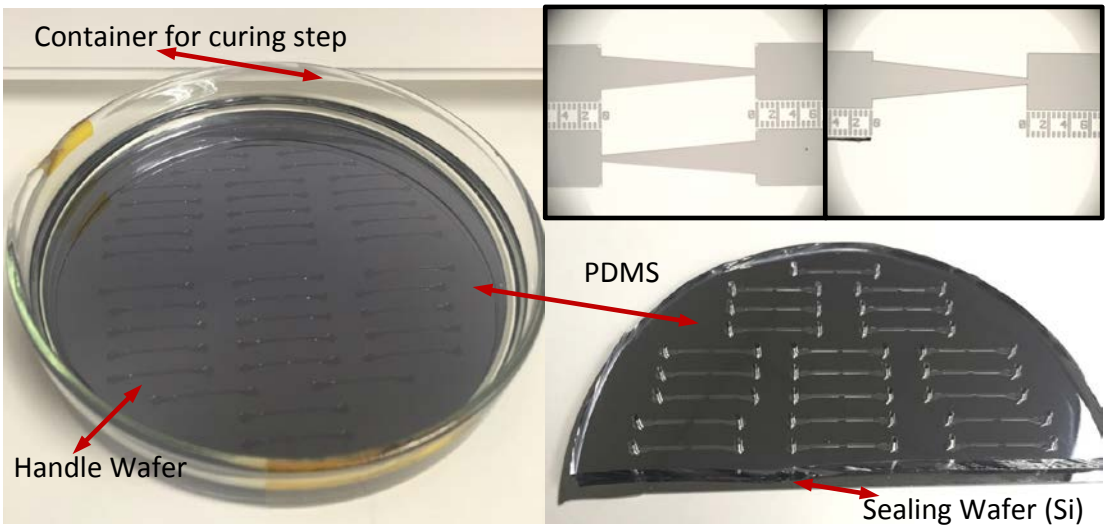


**Figure 4.12: Fabricated diffuser / nozzle single and double channel diffuser test structures.**

**Micropump Fluidic Section (Chamber and Diffuser Elements)**

The molds were created, and PDMS mixture was prepared as explained before. A 3D printed ABS plastic template was used on top of the mold to create the appropriate size and straight-side PDMS microchannel slabs. The template was fixed to the mold with binder clips, each room was filled with PDMS mixture, and left for curing at the room temperature for 48 hours. The room temperature annealing was found better to work for self-bonding by our group [46]. This was the preferred method since an alignment step was needed and bonding could be carried out without an additional adhesion layer. The related pictures are given in Figure 4.13.

After removing the PDMS slabs, inlet-outlet reservoir connections were punctured with a 1.5 mm diameter biopsy punch and cleaned using regular tape for bonding step.

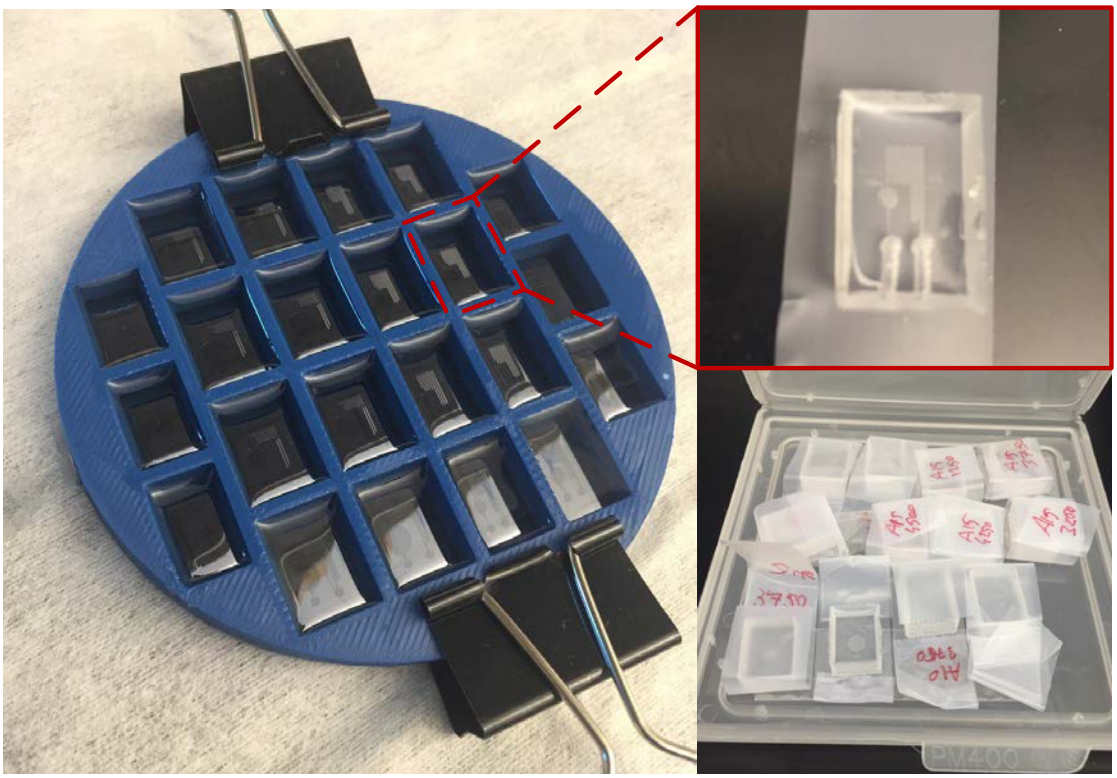

**Figure 4.13: Fabrication of the microchannels. 10:1 ratio of PDMS mixture filled the rooms that are created by 3D-printed template fastened on the SU-8 mold. PDMS microchannel slabs were removed and punctured after 48 hours of curing.**

### 4.3.3. Integration of Membrane-Actuator and Microfluidics

The membrane-actuator section and PDMS fluidic section have to be well aligned for proper working diffusers. Therefore, a probe station and a 3D printed plastic spring loaded apparatus that was designed by our group [47] were used. This apparatus was fixed on the stage of the probe station and kept the PDMS slab stable. Another plastic holder was printed to keep the membrane-actuator devices upside down and safe. Related pictures are given in Figure 4.14.

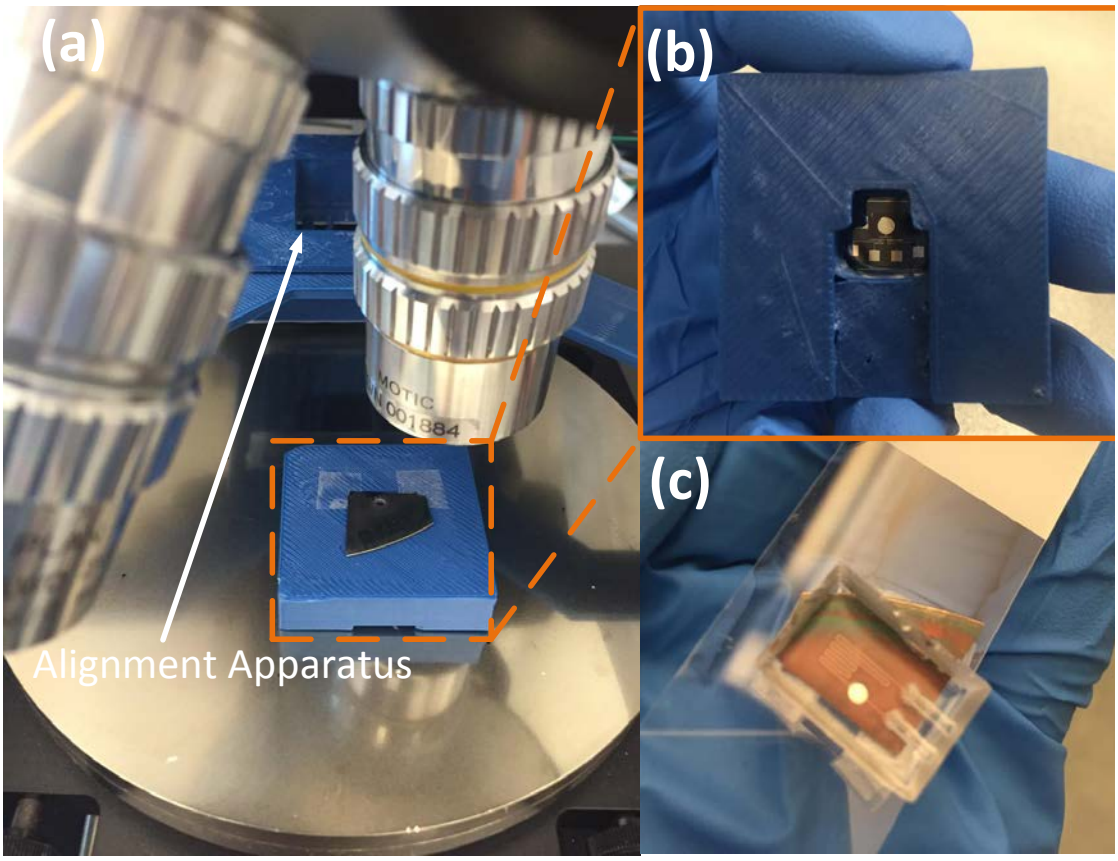


**Figure 4.14: (a) Alignment setup which has 3D printed alignment apparatus and the sample holder. (b) Back side of the 3D printed sample holder. (c) Finalized micropump.**

# CHAPTER 5. EXPERIMENTS

First, the fabricated diffuser elements with various geometries were tested with DIW to optimize the final mask design for microdiffuser and fluidic channels. Afterwards, the ferroelectric and piezoelectric responses of the fabricated actuator devices were tested. Finally, the integrated system consisting of the actuator and microfluidic was tested using colored DIW and methanol.

Testing of the microfluidic section proved to be very challenging. Even a small amount of trapped air inside the channels could seriously affect the experiments. Removing all trapped air from microfluidic channels prior to experiments is essential in order to get accurate data. The next subsections discuss the experiment setups and results of each three experiment sets.

## 5.1. Diffuser / Nozzle Experiments

Initial tests were conducted on fabricated diffuser / nozzle test devices having two asymmetric channels; one for diffuser and another for nozzle in order to observe flow directing capabilities of each fabricated device. The geometry details of the fabricated diffuser valves are given in Table 5.1, where $W$ is the throat width, $L$ is the diffuser length, and $\theta$ is the diverging angle. The colored areas are indicating the fabricated devices. For example $\theta = 6°$ was fabricated for the W100-L1000 sample, but not for the W60-L1000 sample.

**Table 5.1 Length (L), width (W), and angle (θ) values of the fabricated diffuser / nozzle elements. The colored areas indicate the fabricated devices with the corresponding L, W, and θ values.**

| | L=1000 | | | L=1500 | | | L=1200 |
|---|---|---|---|---|---|---|---|
| **θ** | **W60** | **W80** | **W100** | **W60** | **W80** | **W100** | **W120** |
| 6 | | | | | | | |
| 7 | | | | | | | |
| 8 | | | | | | | |
| 9 | | | | | | | |
| 10 | | | | | | | |
| 12 | | | | | | | |
| 15 | | | | | | | |
| 20 | | | | | | | |

The diverging angles were chosen according to the stability map of flat-walled diffusers [10]. The map was not drawn for micro-scaled diffusers, but it can be used to design diffuser geometry with minimal pressure coefficient in the first place. Our experiments proved the usability of the map for micro-scaled devices.

An external UMP3 micropump with a 1mL syringe was used to fill the devices with fluid for testing. Initially, positive pressure was used - meaning that the pump was used at infuse mode. This method resulted in leaks at tubing connections. The leakage issue was overcome by using negative pressure to fill the devices. The outlets of the test devices were connected to the micropump instead of the inlet and working fluid dispensed manually into the inlet reservoir using a syringe as shown in Figure 5.1. The external micropump run at withdraw mode to reduce the air pressure inside the channels resulting in channel filling from the inlet reservoir.

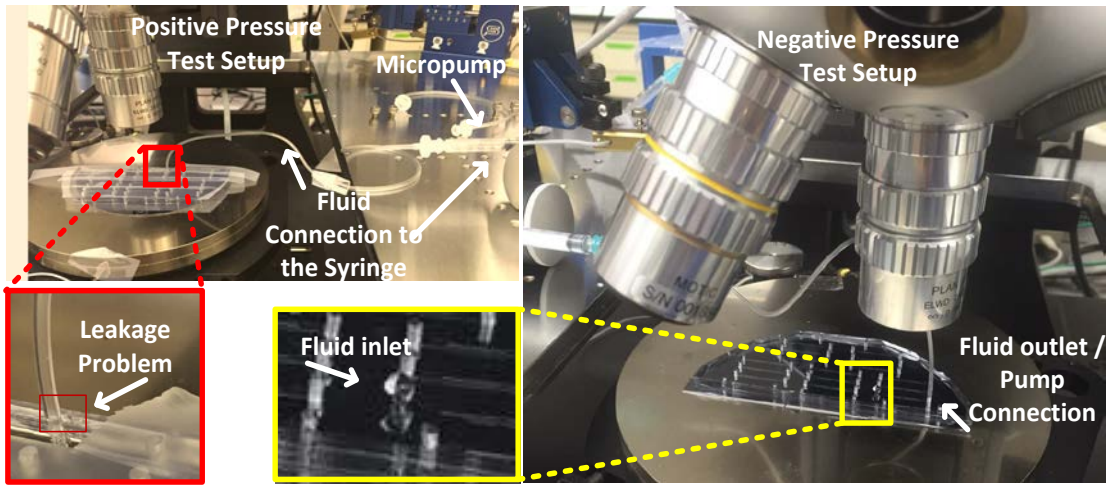


**Figure 5.1: Diffuser element test setups. Leakage observed at inlet is shown in the red box. The yellow box shows a close view of an inlet reservoir which was filled manually using a syringe.**

According to our experiments, all diffuser test elements functioned as expected. However, once the back pressure of a diffuser element was overcome; all fluid flowed into the both channels and blocked the nozzle elements as shown in Figure 5.2. Therefore, we could not obtain comparative results from this setup.

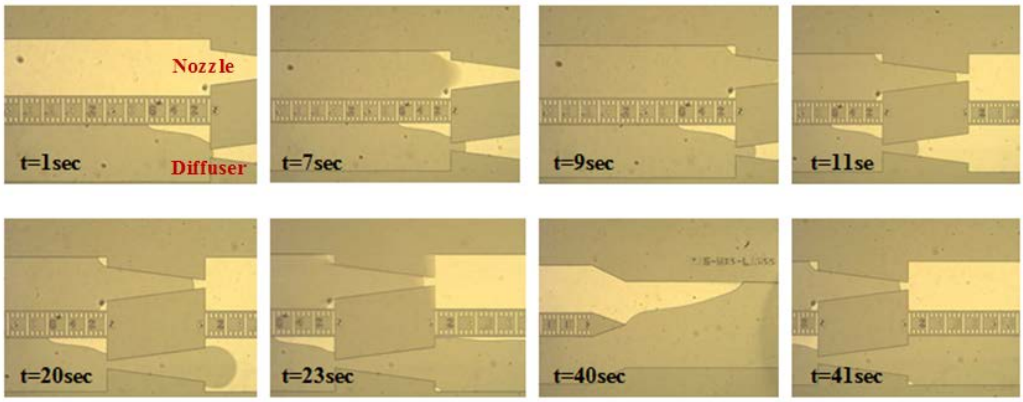


**Figure 5.2: Double channel diffuser / nozzle elements under test. Fluid flow in the nozzle channel stopped due to the fluid coming from the diffuser channel as shown in the figures taken at 40$^{th}$ second and 41$^{st}$ second.**

As mentioned in Chapter 4, the single channel diffuser elements were fabricated from the same mask to overcome the blocking issue. Devices were tested by applying negative pressure and recording videos. In-out times of the fluid to diffuser and nozzle elements were obtained from the videos. The devices were compared according to the in-out time difference at the nozzle and diffuser directions of a device. Since an external pump was used at withdraw mode (negative pressure), the back pressure of the diffuser elements could not be calculated with this setup. Figure 5.3 shows time-laps photos of the test procedure.

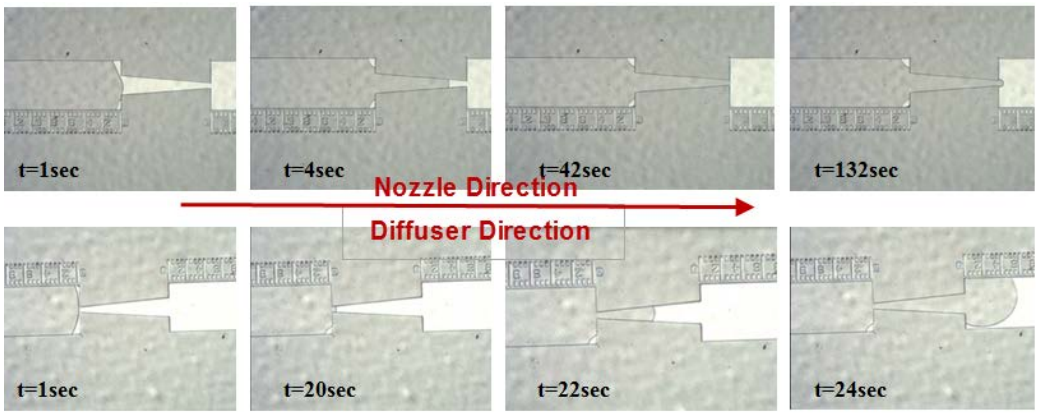


**Figure 5.3: Single channel diffuser tests of L1000-W60-09 device. The fluid was passed the channel in 132 seconds through the nozzle element while in 24 seconds through the diffuser element. The arrow shows the fluid flow direction is through the nozzle for the pictures at the top, and through the diffuser for the pictures at the bottom.**

Another test setup was used to measure back pressures of the devices as shown in Figure 5.4. Water pressure head method was used to measure the maximum pressure that a diffuser valve can handle for forward (diffuser) and reverse (nozzle) flow directions. The pressure difference between the two directions gives the diodicity capability of diffuser valves. A paper ruler with millimeter indentations was taped on a vertical metal surface and magnets were used to move the DIW reservoir precisely and to maintain its

position. The reservoir was filled with DIW up to its brim and connected to the inlet of the test device using a tygon tubing in order to obtain maximum back pressure values for the diffuser. The channels were filled up to a close position to the diffusers using the connected tubing. Then, the reservoir position was raised up by single millimeter steps. The diffusers were monitored closely, and the pressure value when fluid passed through the diffusers was recorded as the maximum pressure value. The same tests were repeated by connecting the tubing to the outlet of the test devices in order to obtain maximum back pressure values for the nozzle elements.

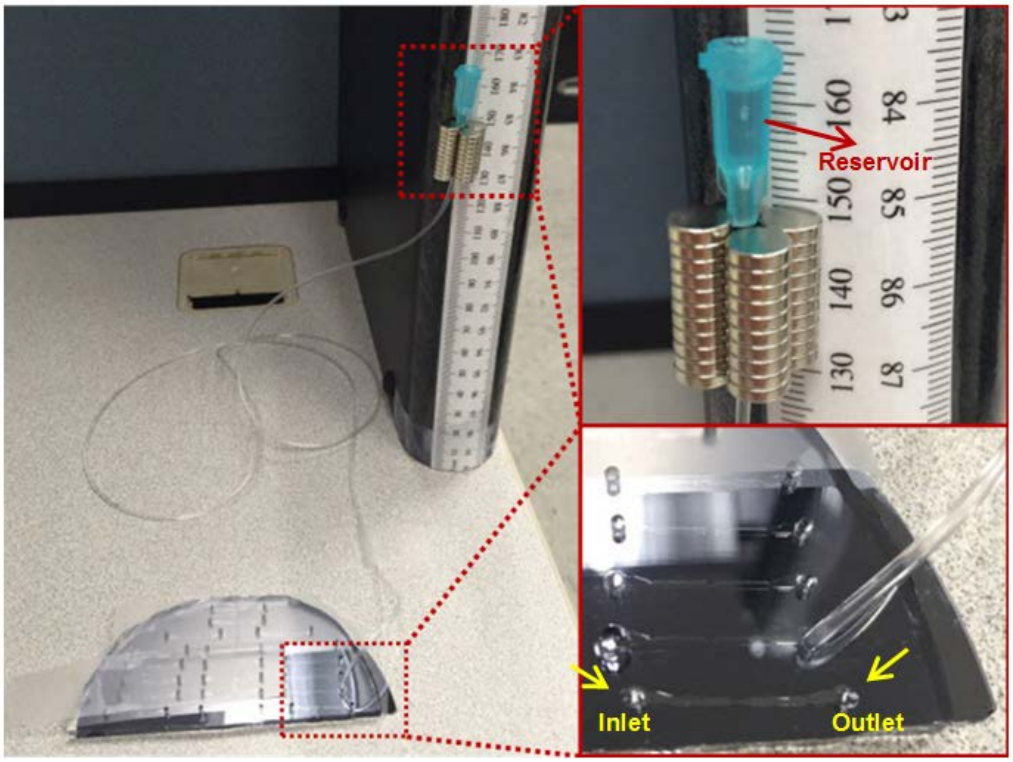


**Figure 5.4: The test setup for back pressure testing of diffusers. Water pressure head method was used to measure the maximum pressure values of a diffuser and nozzle.**

As seen from the converging-wall flow resistance plot in Figure 5.5, the highest back pressures were obtained between angle 9° and 11°. However; there were some

nonlinearity for W=60 samples. While the lowest back pressure values were observed for throat width of 80µm and 100µm samples from angle 6° and 20°, the smallest value was measured from angle 8 for the throat width of 60 µm. Additionally, the value for angle 20° was higher than the average value. This could be caused by very high inlet losses since the samples with 60µm throat width were the smallest ones.

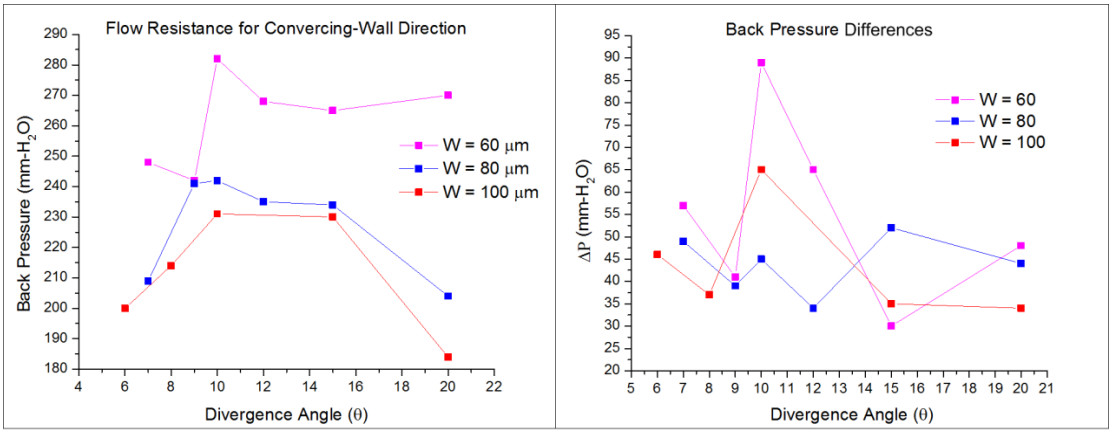


**Figure 5.5: Maximum back pressure results obtained from converging-wall direction (nozzle direction) flow and converging wall pressure difference which is known as diodicity.**

## 5.2. Ferroelectric Experiments

PVDF-TrFE is a ferroelectric material, which means a strong external electric field can reverse its polar axis. However, a piezoelectric device can only be poled once and then keeps the same polarization. Therefore, dynamic ferroelectric properties are not as relevant in piezoelectric devices. On the other hand, some ferroelectric measurements can be useful in order to examine the piezoelectric response. For example, higher remnant polarization means stronger piezoelectric response.

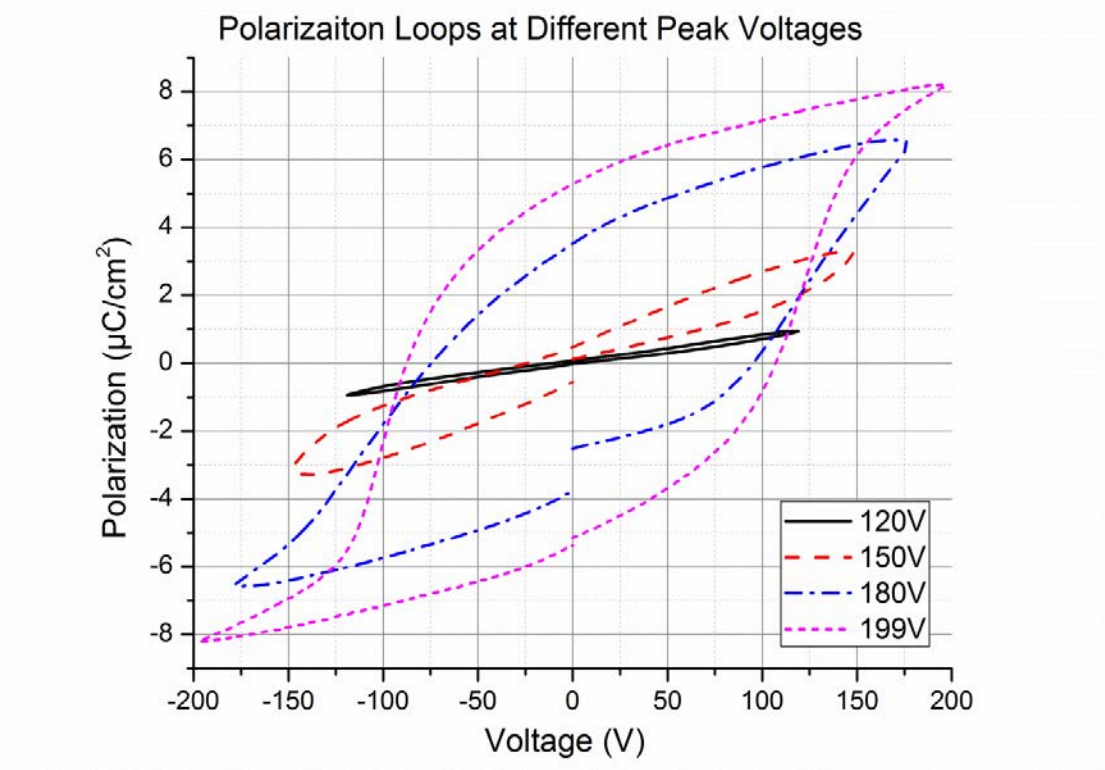


**Figure 5.6: Hysteresis loops obtained from inner electrodes with 0.0103 $cm^2$ area of 1750 µm membrane sample at different peak amplitudes. Remnant polarization was measured as 5.38 $\mu C/cm^2$.**

Hysteresis loops of PVDF-TrFE membrane were obtained using the inner electrodes of the 1750 µm membrane sample with 0.0103 $cm^2$ area at different peak amplitudes. Figure 5.6 shows the hysteresis loops of the PVDF-TrFE membrane. Remnant polarization was measured as 5.38 $\mu C/cm^2$.

### 5.3. Piezoelectric Experiments

The fabricated membranes were poled at room temperature with DC bias using the Radiant Premier II ferroelectric tester. DC bias voltages were applied from 120 V to 200 V in 20 V increments. Applied voltages were kept for 120 seconds, and then zero charging was applied for 30 seconds after each DC step to remove excess trapped charges [42].

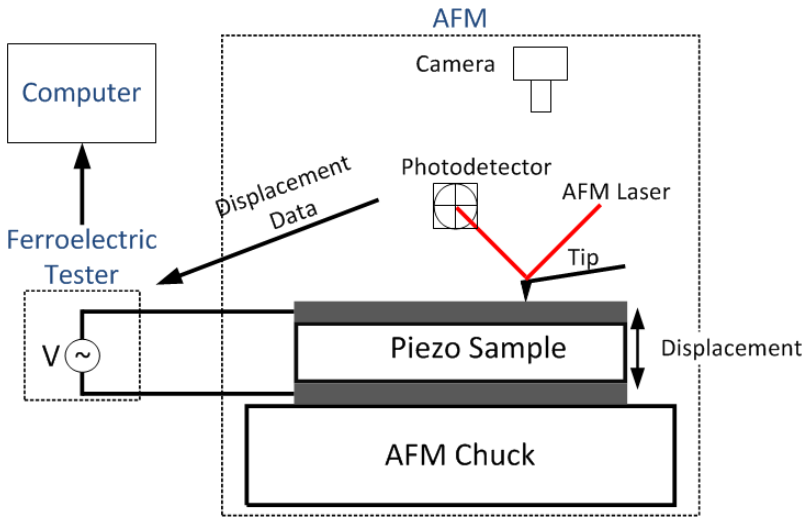


**Figure 5.7: Schematic shows the working principle of PNDS. Resultant piezoelectric displacement generates a proportional signal in the AFM detector by bending the probe. This signal was converted into displacement amplitude.**

After poling the devices, the displacement measurements of the fabricated PVDF-TrFE actuators were performed using a PNDS (Precision Nano Displacement System) and ferroelectric tester. This is a system designed to measure nanometer-scale piezoelectric displacements. A schematic that shows the working principle of PNDS is shown in Figure 5.7.

First, the AFM probe was brought into contact with the sample. Then, an AC signal was applied to the sample by the ferroelectric tester as shown in Figure 5.8. Resultant piezoelectric displacement generates a proportional signal in the AFM detector by bending the probe, which is fed back to the tester for processing. Detector signal was converted into displacement amplitude using the data obtained from force-distance curves of the AFM.

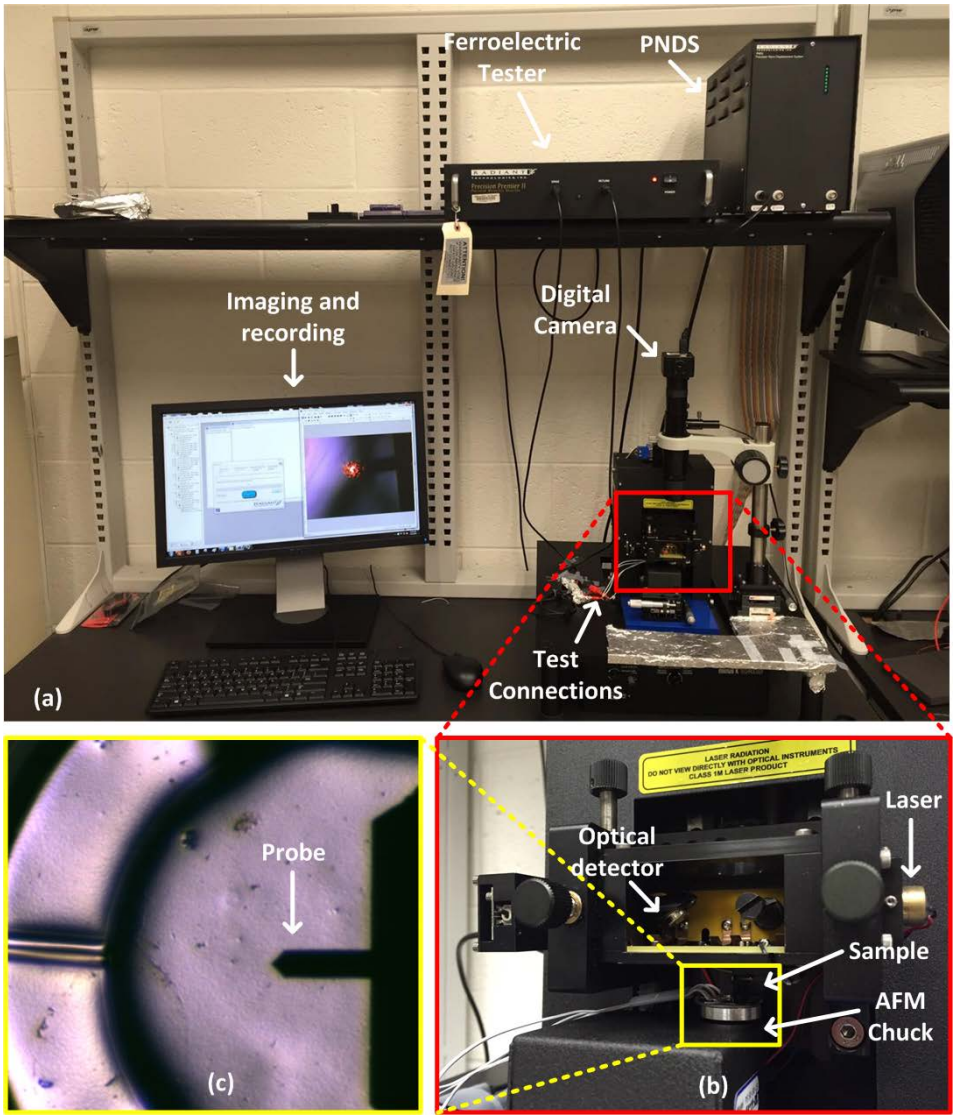


**Figure 5.8: (a) Test setup with a sample placed on the AFM chuck for the displacement measurements of the membranes. (b) Close-up view of the AFM chuck and tested device. (c) Microscope picture of the sample and the probe.**

Displacement measurements were taken from the 1750 µm and 2500 µm in diameter actuators at 20 V. Displacement color maps obtained from the piezoelectric tests are shown in Figure 5.9. Displacement data were taken from 36 different points of the membranes as shown in Figure 5.9-(c). The maximum displacements were measured as 199 nm from the Φ1750 sample, and ~350 nm from the Φ2500 sample at 20V. The

maximum displacements obtained from the samples were almost three times higher than FEM simulation results. Possible reasons for this discrepancy are: difference between actual residual stress and residual stress information fed to the simulated model and/or the unintentional loss in the thickness of inactive PVDF-TrFE layer during DRIE process.

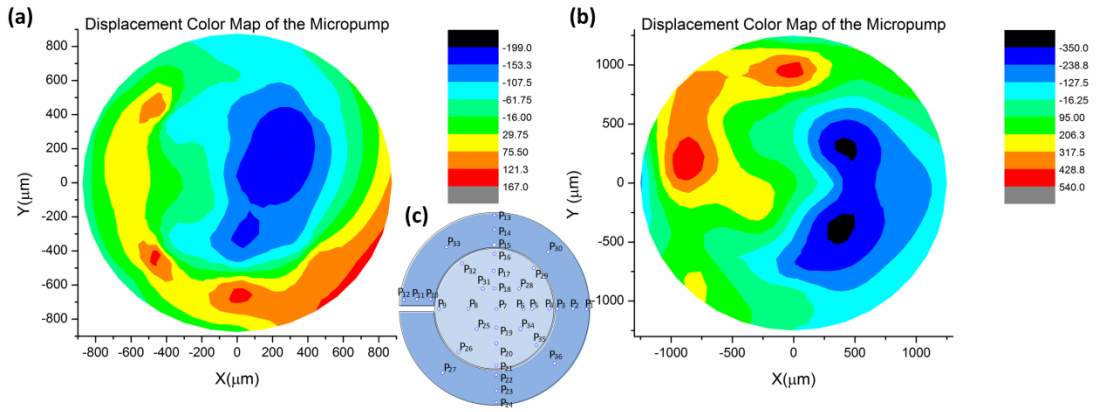


**Figure 5.9: The displacement results taken form (a) 1750 µm in diameter actuator and (b) 2500 µm in diameter actuator at 20 V. (c) The 36 points that the measurements were taken from. A maximum 199 nm displacement was observed near the center of D1750 sample, while 350 nm was measured for D2500 sample.**

## 5.4. Microfluidic and Actuator-Membrane Integration

Actuators and microfluidic channels were bonded as explained in section 4.3. However, it was a very challenging task since the backside of the substrate was not polished. Rough surface does not reflect sufficient microscope light resulting in difficulties while alignment. Figure 5.10 shows the microscope images of the fabricated microchannels.

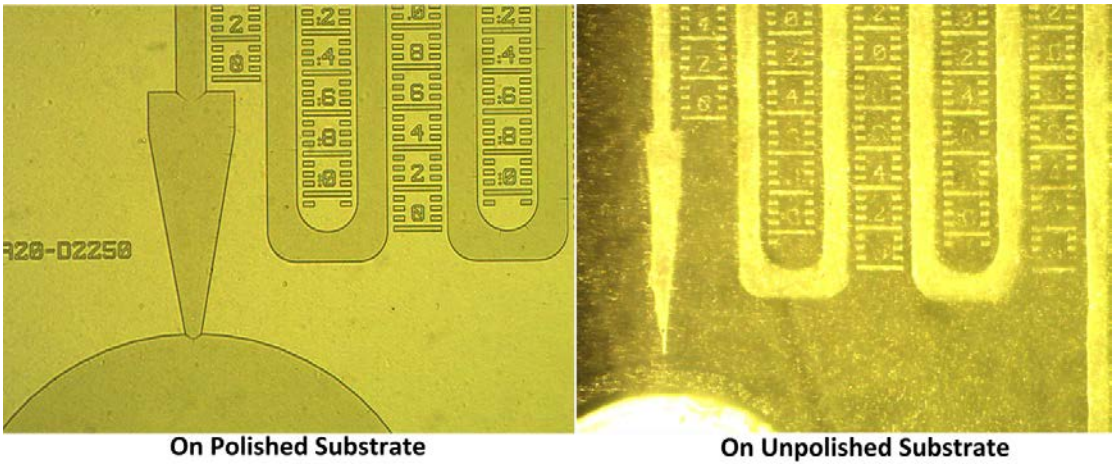


**Figure 5.10: The visibility of the fabricated microchannels on polished and unpolished substrates. Since the chamber boundaries were not discernible, extra attention was needed for proper bonding.**

The device, which had a diameter of 1750 μm, was connected to a signal generator and its reservoir was filled with DIW. Initially, small voltages (5 V-20 V peak-to-peak) were applied at low frequencies and no fluid movement was observed. It was necessary to increase excitation voltage beyond 20 V to understand the reason for no fluid flow. Ferro electric tester was used to provide higher signals to the device since the signal generator cannot supply more than 20 V. The picture of the test setup is given in Figure 5.11. Tests were repeated by applying increasing voltage up to 80V. No fluid movement was observed during the tests. However, the actuator movements at even 5 V can be clearly seen under microscope.

Additional FEM study was made to understand the inability to observe fluid pumping in the integrated system. Since the integrated system was tested upside down, the actuator pressure must be higher than the initial pressure of the fluid inside the 500 μm-deep channel. Approximately 9.5 Pa back pressure was obtained from the simulations for the Φ1750 sample, which is almost twice as much as the water pressure inside the

chamber. Therefore, it is proven that the fluid pumping inability was not caused by the fluid pressure inside the chamber.

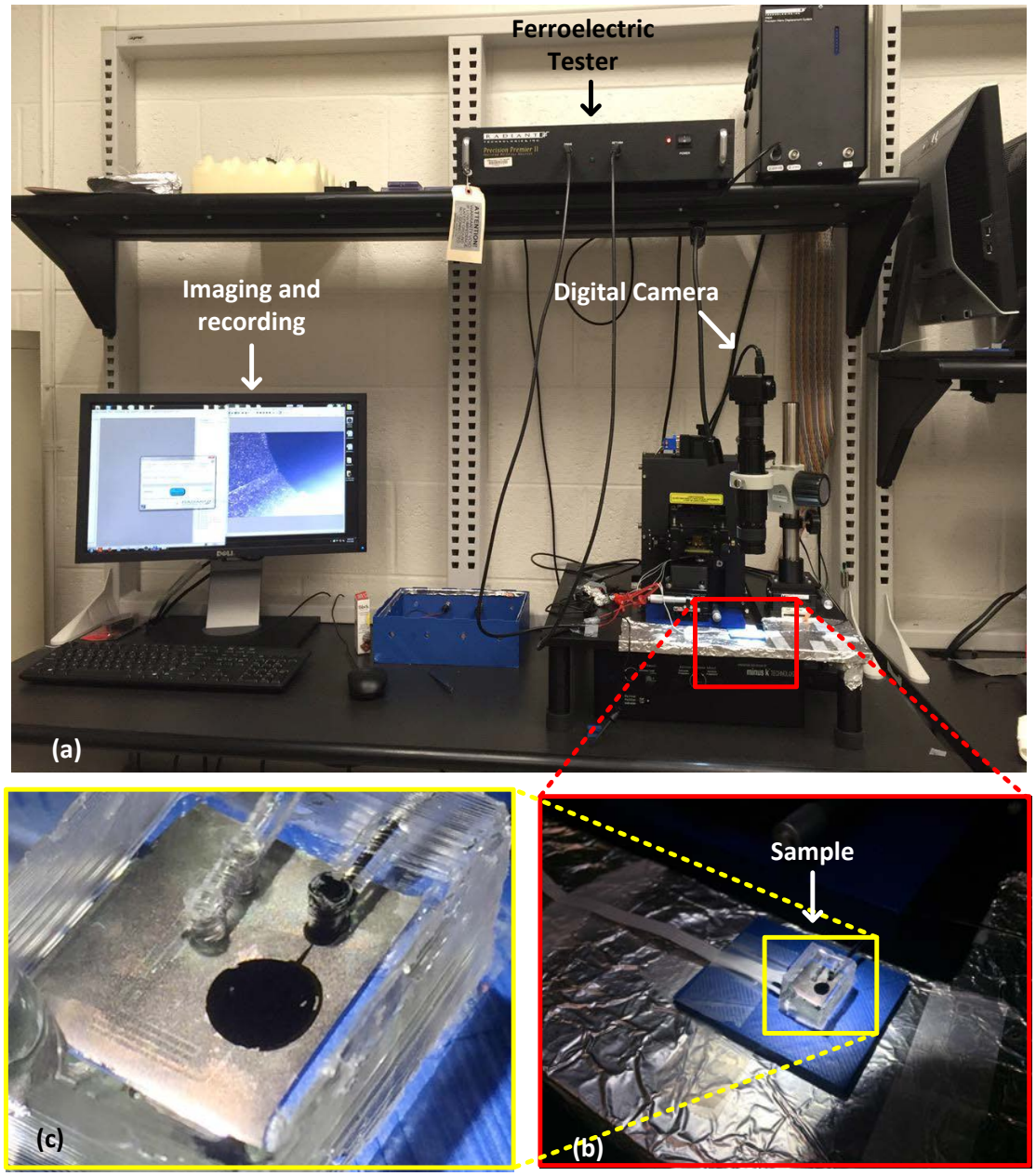


**Figure 5.11: The test setup for the full micropump system. Ferroelectric tester was used to give actuation signal and the digital camera was used to monitor the fluid flow.**

Since the visibility of the channels was not good, it was almost impossible to see the flow of DIW. Therefore, black colored DIW was used as working fluid. Trapped air regions were observed in the chamber as shown in Figure 5.11 and Figure 5.12. This is a well-known challenge in microfluidics, and possible reason of the fluid pumping inability. These trapped air regions inside the chamber can eliminate the effect of volume change generated by the actuator. In additional to this, high losses at the diffuser throats due to the hydrophobicity of PDMS can also cause the pumping inability. In order to resolve these issues, surface treatment is necessary to make the PDMS channels hydrophilic.

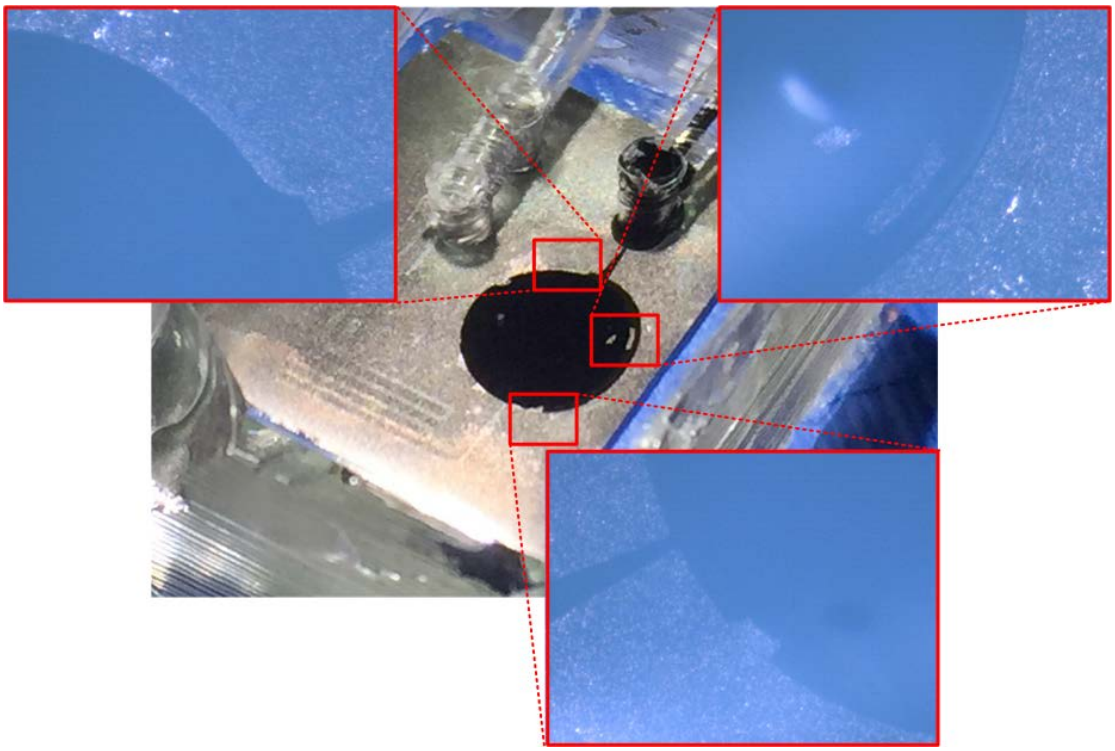

**Figure 5.12: Pictures of the trapped air regions inside the chamber. These regions can majorly affect the pump efficiency.**

## CHAPTER 6. CONCLUSION AND FUTURE WORK

This thesis presents a fully biocompatible miniature micropump system consisting of a novel actuator-membrane structure and fluidic channels with fluid directing elements. This device possesses the potential to be integrated with implantable high precision therapeutic drug delivery devices to deliver precise nanoliter scale volumes of fluidic samples

Wide variety of PDMS diffuser / nozzle elements for microfluidic applications were fabricated and experimentally tested using DIW. The highest back pressure difference between nozzle and diffuser directions, which gives the diodicity capacity of the diffuser elements, were obtain around angle 9.5° for diffuser length of 1000μm. Additionally, very low back pressure difference was observed from the samples with higher than 15° diverging angle as expected. The highest back pressure difference (~90 mm-$H_2O$) was obtained from the sample with 10° diverging angle, 60 μm throat width and 1000 μm diffuser length.

Finite element modeling (FEM) for the actuator-membrane section was performed to optimize the geometry and materials of the micropump. As result of FEM simulations, PVDF-TrFE showed the most promising results as both actuator and membrane material.

A novel actuator-membrane structure was fabricated from a piezoelectric polymer polyvinylidene fluoride-trifluoroethylene (PVDF-TrFE). Its ferroelectric response was examined and the remnant polarization of the film was measured as 5.38 μC/$cm^2$. The piezoelectric response of the devices was measured using a PNDS and ferroelectric tester. The maximum displacements around the center were measured as 199 nm and 340 nm for the samples with 1750 μm and 2500 μm diameter at 20 V. The measured displacement

values are higher than the simulation results. This is most likely caused by the difference between the actual residual stress of the film and the value that was used in the simulations.

Full operation of actuator-membrane structures and diffuser elements which are the two components of the designed micropump was successfully proven separately and integration of these components was demonstrated. Unfortunately, the fluid flow could not be observed while the actuator was working properly under tests with working fluid. In order to understand fluid behavior, black colored DIW was used and trapped air regions were observed inside the chamber. These trapped air regions eliminates the effect of volume change generated by the actuator. Hydrophilization of PDMS microfluidic section for future work is necessary in order to fill the channel properly and minimize the trapped air regions. Additionally, this can help to reduce the inlet losses at diffuser throats which are the other possible reason of the pumping inability of the integrated system.

## REFERENCES


1. Olsson, A., *Valve-less diffuser micropumps*. 1998.

2. Amirouche, F., Y. Zhou, and T. Johnson, *Current micropump technologies and their biomedical applications.* Microsystem Technologies, 2009. 15(5): p. 647-666.

3. Meng, E., *MEMS technology and devices for a micro fluid dosing system*. 2003, Citeseer.

4. Polla, D.L., et al., *Microdevices in Medicine 1.* Annual Review of Biomedical Engineering, 2000. 2(1): p. 551-576.

5. Smits, J.G., *Piezoelectric micropump with microvalves*. 1990, Google Patents.

6. Tay, F.E., *Microfluidics and BioMEMS applications*. 2002: Springer.

7. Nisar, A., et al., *MEMS-based micropumps in drug delivery and biomedical applications.* Sensors and Actuators B: Chemical, 2008. 130(2): p. 917-942.

8. Tsai, N.-C. and C.-Y. Sue, *Review of MEMS-based drug delivery and dosing systems.* Sensors and Actuators A: Physical, 2007. 134(2): p. 555-564.

9. Laser, D. and J. Santiago, *A review of micropumps.* Journal of Micromechanics and Microengineering, 2004. 14(6): p. R35.

10. White, F.M., *Fluid Mechanics,(2003)*. 2003, McGraw-Hill.

11. Nakamachi, E., et al., *Development of a micropump for Bio-MEMS using a new biocompatible piezoelectric material MgSiO3.* Journal of Micro/Nanolithography, MEMS, and MOEMS, 2011. 10(3): p. 033013-033013-7.

12. Pabst, O., et al., *Inkjet printed micropump actuator based on piezoelectric polymers: Device performance and morphology studies.* Organic Electronics, 2014. 15(11): p. 3306-3315.

13. Pabst, O., et al., *All inkjet-printed piezoelectric polymer actuators: Characterization and applications for micropumps in lab-on-a-chip systems.* Organic Electronics, 2013. 14(12): p. 3423-3429.

14. Johari, J., J. Yunas, and A.A. Hamzah, *Piezoelectric micropump with nanoliter per minute flow for drug delivery systems.* Sains Malaysiana, 2011. 40(3): p. 275-281.

15. Zhou, Y. and F. Amirouche, *An electromagnetically-actuated all-PDMS valveless micropump for drug delivery.* Micromachines, 2011. 2(3): p. 345-355.

16. Singh, S., et al., *Analytical modeling, simulations and experimental studies of a PZT actuated planar valveless PDMS micropump.* Sensors and Actuators A: Physical, 2015. 225: p. 81-94.

17. Wang, X.Y., et al., *A compact and high flow-rate piezoelectric micropump with a folded vibrator.* Smart Materials and Structures, 2014. 23(11): p. 115005.

18. Xu, T.-B. and J. Su, *Development, characterization, and theoretical evaluation of electroactive polymer-based micropump diaphragm.* Sensors and Actuators A: Physical, 2005. 121(1): p. 267-274.

19. Zhang, T. and Q.-M. Wang, *Valveless piezoelectric micropump for fuel delivery in direct methanol fuel cell (DMFC) devices.* Journal of Power Sources, 2005. 140(1): p. 72-80.

20. Fadl, A., *Valve-less Rectification Micropumps Based on Bifurcation Structures*. 2010.

21. Zhang, T. and T. Cui. *High-performance surface-tension-driven capillary pumping based on layer-by-layer self assembly of TiO 2 nanoparticles*. in *2011 16th International Solid-State Sensors, Actuators and Microsystems Conference*. 2011. IEEE.

22. Tsai Jr, -.H. and L. Lin, *A thermal-bubble-actuated micronozzle-diffuser pump.* Journal of Microelectromechanical Systems, 2002. 11(6): p. 665-671.

23. Trolier-McKinstry, S. and P. Muralt, *Thin film piezoelectrics for MEMS.* Journal of Electroceramics, 2004. 12(1-2): p. 7-17.

24. Wang, H.-H., et al. *A light-activated optopiezoelectric thin-film actuator for microfluidic applications*. in *SPIE BiOS*. 2015. International Society for Optics and Photonics.

25. Xu, T.-B. and J. Su, *Design, modeling, fabrication, and performances of bridge-type high-performance electroactive polymer micromachined actuators.* Journal of Microelectromechanical Systems, 2005. 14(3): p. 539-547.

26. Kuoni, A., et al., *Polyimide membrane with ZnO piezoelectric thin film pressure transducers as a differential pressure liquid flow sensor.* Journal of Micromechanics and Microengineering, 2003. 13(4): p. S103.

27. Junwu, K., et al., *Design and test of a high-performance piezoelectric micropump for drug delivery.* Sensors and Actuators A: Physical, 2005. 121(1): p. 156-161.

28. Izzo, I., et al., *Modeling and experimental validation of a piezoelectric micropump with novel no-moving-part valves.* Sensors and Actuators A: Physical, 2007. 133(1): p. 128-140.

29. Wang, D.-A. and H.-H. Ko, *Piezoelectric energy harvesting from flow-induced vibration.* Journal of Micromechanics and Microengineering, 2010. 20(2): p. 025019.

30. Chandrasekaran, A. and M. Packirisamy, *Geometrical tuning of microdiffuser/nozzle for valveless micropumps.* Journal of Micromechanics and Microengineering, 2011. 21(4): p. 045035.

31. Yang, K.-S., et al., *A comparative study of nozzle/diffuser micropumps with novel valves.* Molecules, 2012. 17(2): p. 2178-2187.

32. Olsson, A. and E. Stemme, *Diffuser-element design investigation for valve-less pumps.* Sensors and Actuators A: Physical, 1996. 57(2): p. 137-143.

33. Chen, Y.-T., et al., *Fabrication and investigation of PDMS micro-diffuser/nozzle.* Journal of Materials Processing Technology, 2008. 198(1): p. 478-484.

34. Wang, Y.-C., et al., *Loss characteristics and flow rectification property of diffuser valves for micropump applications.* International Journal of Heat and Mass Transfer, 2009. 52(1): p. 328-336.

35. Singhal, V., S.V. Garimella, and J.Y. Murthy, *Low Reynolds number flow through nozzle-diffuser elements in valveless micropumps.* Sensors and Actuators A: Physical, 2004. 113(2): p. 226-235.

36. Olsson, A., et al., *Micromachined flat-walled valveless diffuser pumps.* Journal of Microelectromechanical Systems, 1997. 6(2): p. 161-166.

37. Jiang, X., et al., *Micronozzle/diffuser flow and its application in micro valveless pumps.* Sensors and Actuators A: Physical, 1998. 70(1): p. 81-87.

38. Olsson, A., G. Stemme, and E. Stemme, *Numerical and experimental studies of flat-walled diffuser elements for valve-less micropumps.* Sensors and Actuators A: Physical, 2000. 84(1): p. 165-175.

39. Olsson, A., G. Stemme, and E. Stemme. *Simulation studies of diffuser and nozzle elements for valve-less micropumps*. in *Solid State Sensors and Actuators, 1997. TRANSDUCERS'97 Chicago., 1997 International Conference on*. 1997. IEEE.

40. Yamahata, C., et al., *A PMMA valveless micropump using electromagnetic actuation.* Microfluidics and Nanofluidics, 2005. 1(3): p. 197-207.

41. Sakai, T., S. Hoshiai, and E. Nakamachi, *Biochemical compatibility of PZT piezoelectric ceramics covered with titanium thin film.* Journal of Optoelectronics and Advanced Materials, 2006. 8(4): p. 1435.

42. Toprak, A. and O. Tigli, *MEMS Scale PVDF-TrFE-Based Piezoelectric Energy Harvesters.* Journal of Microelectromechanical Systems, 2015. 24(6): p. 1989-1997.

43. Toprak, A. and O. Tigli, *Interdigitated-electrode-based mems-scale piezoelectric energy harvester modeling and optimization using finite element method.* Ultrasonics, Ferroelectrics, and Frequency Control, IEEE Transactions on, 2013. 60(10): p. 2162-2174.

44. Kim, S., W.W. Clark, and Q.-M. Wang, *Piezoelectric energy harvesting with a clamped circular plate: analysis.* Journal of Intelligent Material Systems and Structures, 2005. 16(10): p. 847-854.

45. Guodong, Z. *Multi-step spin coating method to improve ferroelectric P (VDF-TrFE) thin film quality*. 2011.

46. Gajasinghe, R., et al., *Experimental study of PDMS bonding to various substrates for monolithic microfluidic applications.* Journal of Micromechanics and Microengineering, 2014. 24(7): p. 075010.

47. Senveli, S.U., *Novel Acoustic Wave Microsystems for Biophysical Studies of Cells.* 2016.